Impact and multi-impact performance of prestressed CFRP strengthened RC beams using novel H-type end anchor

Zhenyu HUANG[1,2,3], Weixiong DENG[1,2], Ren LI[1,2], Zenghui YE[1,2], Yingwu ZHOU[1,2*], Debo ZHAO[2], Jianqiao YE[4]

1 Guangdong Provincial Key Laboratory of Durability for Marine Civil Engineering, Shenzhen University, Shenzhen, China 518060.

2 College of Civil and Transportation Engineering, Shenzhen University, Shenzhen, China 518060.

3 Key Laboratory of Impact and Safety Engineering, Ministry of Education, Ningbo University, Ningbo, China 315211

4 Department of Engineering, Lancaster University, Lancaster, UK, LA1 4YR.

Abstract

To address the problem of insufficient ductility of traditional CFRP reinforced concrete beams and to enhance the application of CFRP in engineering structures, the present study develops a novel prestressed CFRP strengthened RC beams using H-type end anchor with ductility controllable device. In this device, the reinforced bars (part of that) are replaced by CFRP which is prestressed as the structural enhancement material. The CFRP sheet is connected with a tensioned screw which is used to realize the function of early warning through a large plastic deformation when the structure is overloaded. Thus, the ductility of the composite structure could be significantly improved by yielding of the screw rod rather than the fracture failure of CFRP sheet. This study investigates the flexural static and impact performance including the failure mechanism, load-displacement curves, energy consumption capability, and impact responses of the large-scaled RC beams strengthened by prestressed CFRP through four-point bending and drop-weight impact. The test results show that the specimens fail in flexural with distributed vertical cracks in the bending region under static and impact test. The screw-bar yielded after impact loads, resulting in a satisfied ductile behavior of such composite beam. The novel device developed in this study provides a new approach to address the design deficiency with insufficient ductility behavior while using CFRP as strengthening material. The prestressing technology can be used to take advantage of the material efficiency of the high strength CFRP, and opens a new way for CFRP application in civil engineering.

Keywords: CFRP; impact performance; post-impact; prestressed structures; FRP-concrete.

Corresponding author. Tel: +86-8697-5402; Fax: +86-2673-2850; Email: xxx@szu.edu.cn

1. Introduction

Fiber reinforced polymer (FRP) strengthening improves the bearing capacity, ductility and seismic performance of the concrete structures [1, 2], especially its high corrosion resistance promotes its application in marine infrastructures. Most studies on FRP-reinforced concrete structures particularly focused on the mechanical behavior, failure mechanism, ultimate resistance and seismic performance of FRP strengthened damaged concrete structures or new built structures [3, 4]. There are two major obstacles in the large-scale application of FRP materials in engineering structures :(1) the higher one-time investment of FRP compared to conventional steel reinforcement [5]; (2) FRP is a linear brittle material with high tensile strength and small fracture strain, which leads to various failures such as interface peeling, tensile fracture of FRP material and combined failures. These non-ductile failure modes of FRP material significantly reduce the structural ductility [6, 7]. Therefore, it is of great importance to address the ductility issue of FRP materials in a structural way in new built FRP-concrete composite structures and FRP strengthened structures.

The superior mechanical and durable properties of FRP enable to from various types of new composite sections, e.g., FRP confined concrete, FRP-concrete-steel tube composite column. This could be widely used in the repaired bridge RC columns with wrapped FRP, composite pipelines in the water, protective walls, and etc. [8-10]. In these engineering applications, extensive key structural components are exposed to frequent or occasional impact loads, e.g., the vehicle impact, heavy rockfalls, wave impact, hull impact and even explosion [11, 12]. Under these extreme loads in the marine environment, the impact resistance, failure mechanism and the corresponding damage of FRP-reinforced concrete members are far more unclear [13, 14]. As the impact load generates extremely high stress on the structure within a short time, the effect of high strain rate on the mechanical response of concrete and FRP materials as well as the bond behavior of FRP-concrete interface cannot be ignored [15]. The main index to evaluate the impact resistance of the structure lies in the energy dissipation of the structure, while the component ductility serves as an important target of the energy dissipation capacity. Therefore, to improve the ductility and energy dissipation capacity of FRP-concrete composite structures efficiently is an urgent research topic.

To overcome the problem of insufficient ductility of traditional FRP repaired RC beams, the present study develops a novel hybrid single-bar fuse structure reinforced by prestressed CFRP with well-controlled ductility manner for RC structures. The novel fuse structure utilizes the prestressed CFRP sheet to replace the reinforced bar (or part of them) as structural reinforcing mate-

Corresponding author. Tel: +86-8697-5402; Fax: +86-2673-2850; Email: xxx@szu.edu.cn

rial connected with the tensioning screw rod. A large plastic deformation is formed by yielding of screw rod to trigger the safety warning when the structure is overloaded. Therefore, the ductility of the whole structure has been promoted significantly. This study systematically investigates the load transfer mechanism and composite action between the novel fuse structure for RC beams strengthened by prestressed CFRP, and verify the enhancement efficiency and stability of the structural system subjected to impact loads. The static flexural resistance, flexural impact ductility and energy dissipation capacity, and the damage evolution mechanism of the composite beam through static and multiple impact tests were evaluated respectively. Finally, a multi-objective design procedure of the flexural and impact resistance is presented for the novel hybrid single-bar fuse structures.

2. Experiments

2.1 Specimens

2.1.1 Design of novel hybrid fuse structure with prestressed CFRP

The experimental program consists of two types of specimens, including the normal reinforced concrete beam and prestressed CFRP strengthened concrete beam using the novel fuse structure as shown in Fig 1. The hybrid fuse structure is made of the two fixed plates mounted in the concrete, CFRP sheet, self-locking plate and screw-rod. The prestress on CFRP is applied by using the hydraulic jack through the screw-rod and prestress anchor as the reaction substrate. When the designed prestress is achieved, the blot nuts are fastened on the screw-rod at the fixed plate while the redundant screw-rod is cut off and the prestressed anchor is demounted. It is noted that the self-locking plate is mounted by using blind blots with slot holes, thus this plate is moveable while prestressing. The CFRP sheet can be self-locked around this plate, which is automatically fastened while prestressing. The detailed structure and installation procedures of the fuse structure with prestressed CFRP sheet is shown in Figure 1.

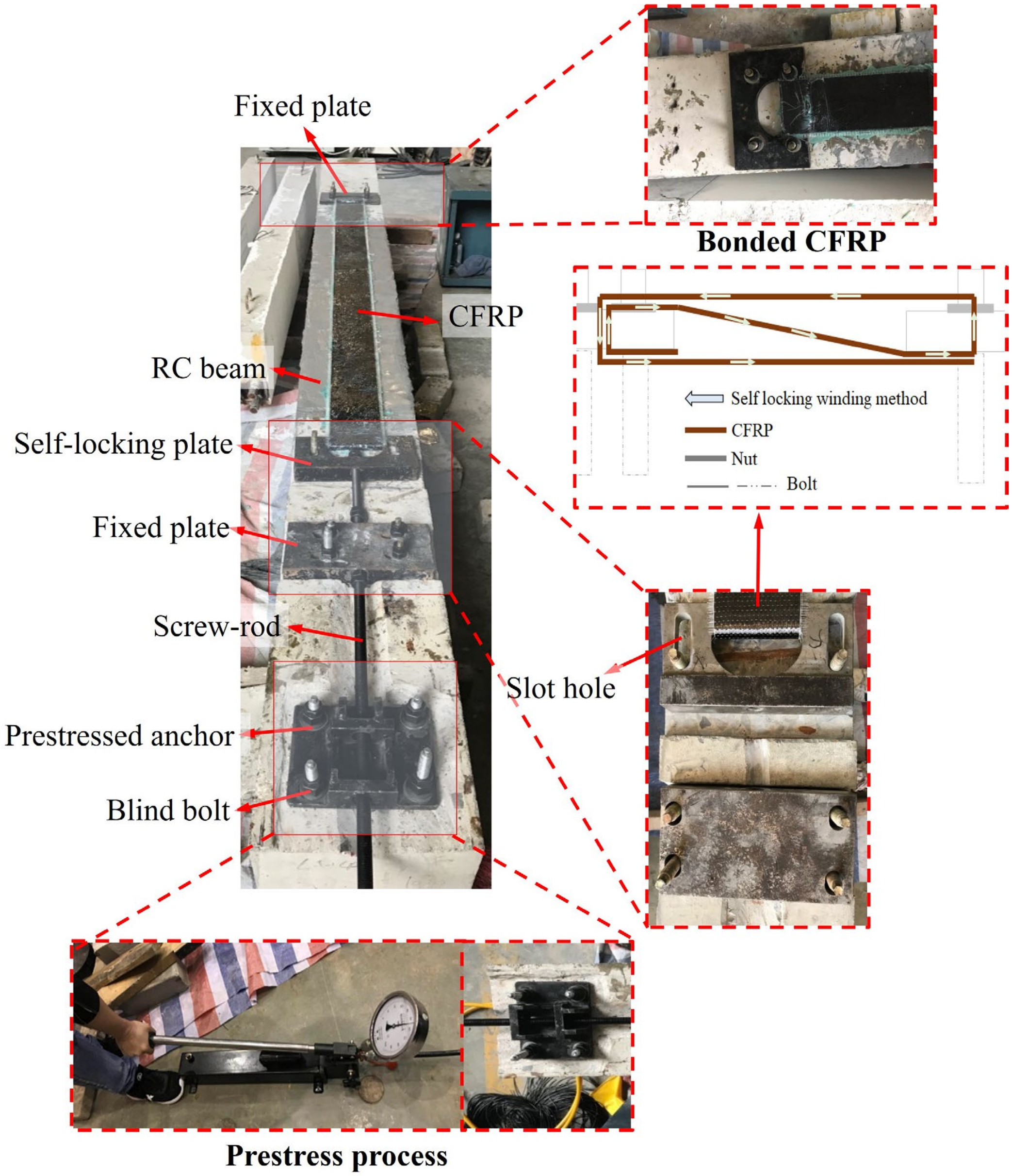

Figure 1 Detailed fuse structure with prestressed CFRP.

2.1.2 Materials

The concrete used in the RC beams is commercial concrete with compressive strength grade of C25. The mixture ratio of the concrete is shown in Table 1, with the water/cement ratio and sand ratio of 0.47 and 0.32, respectively. All the reinforced concrete beams required for the test were cast in one batch with 100×100×100 mm concrete cube samples prepared for concrete strength evaluation. The measured compressive strength of concrete at testing day was 22.7MPa.

Table 1 Mix proportion of concrete

Cement	Water	Sand	Coarse aggregate	W/C ratio	Compressive strength (MPa)
1	0.47	1.59	3.39	0.47	22.7

The specific material properties of the used CFRP sheet and high-performance epoxy are shown in Tables 2 and 3. The mechanical proprieties were determined by the tensile test on the CFRP samples. Figure 2 shows the stress-strain curves of CFRP.

Table 2 Mechanical properties of CFRP sheet

FRP	Tensile strength (MPa)	Elastic modulus (GPa)	Elongation (%)	Thickness (mm)
CFRP sheet	3300	230	1.7	0.167

Table 3 Martial properties of adhesive

Compressive strength (MPa)	Tensile strength (MPa)	Bending strength (MPa)	Elongation (%)	Tensile modulus (MPa)
79.4	55.6	95.7	2.2	3314.2

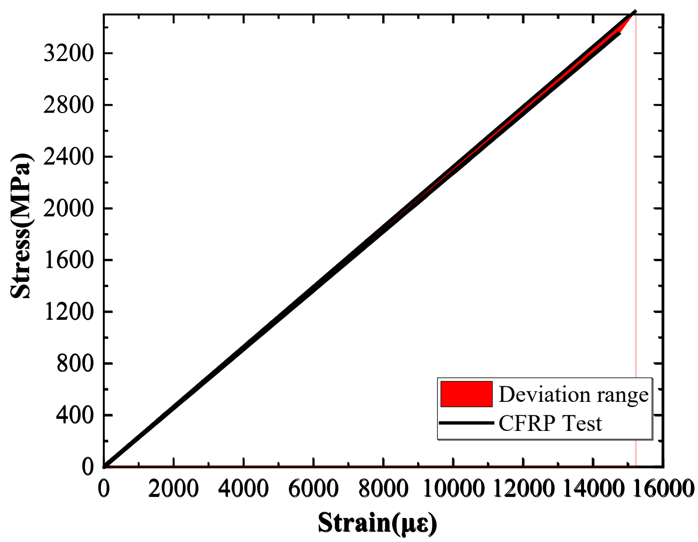

Figure 2 Stress-strain curve of CFRP

In the test, the ductile screw-rods (also called "fuse" in present study) with diameters of 14mm, 16 mm and 18 mm are used to connect the self-locking plate and fixed plate. The prestress is applied through the screw-rod using the prestressed anchor as reaction substrate. The mechanical properties of the steel screw-rods are shown in Table 4. The longitudinal reinforcing bars and stirrups used in RC beams are HRB400 and HRB335 grade ribbed bars. To investigate the influence of different reinforcement ratio on the flexural behavior of the prestressed CFRP composite beams, longitudinal rebars with diameter of 16 mm and 22 mm and stirrups with a diameter of 10 mm are selected. The mechanical properties of reinforcement are obtained through standard tensile tests. Table 5 presents the mechanical properties of the reinforcement.

Table 4 Mechanical properties of screw-rod and reinforcement

Steel type	ID	Elastic modulus (GPa)	Yield strength (MPa)	Tensile strength (MPa)
Screw rod	SR14	210.0	472.0	612.0
	SR16	210.0	437.5	547.0
	SR18	210.0	572.5	699.5
Reinforcement	D10	198.2	382.2	536.6
	D16	197.8	437.5	580.0
	D22	204.3	441.0	584.1

2.1.3 Test specimens

The experimental program consists of two types of full-scale RC beam, including the normal RC beams and prestressed CFRP strengthened RC beam using the novel fuse structure as shown in Figure 1. All these specimens are made of the same concrete grade C25. The prestress process of CFRP sheet employs the hydraulic jack. The test program designs four RC beams for static four-point bending test while three are for drop-weight impact tests. Table 6 shows the design parameters for the specimens while Figure 3 shows the dimension and detailing of specimens.

Table 6 Design parameters of the test specimens.

Loading type	Specimen ID	B (mm)	d (mm)	n	f_c (MPa)	ρ(%)	μ (MPa)	Bond
Static	LA-0	-	-	-	C25	1	0	nil
	LA-1	100	18	6	C25	1	800	nil
	LA-2	100	18	6	C25	1	800	Yes
	LA-3	100	16	6	C25	1	1000	nil
Impact	NB-896-2.7	-	-	-	C25	1	-	nil
	PB16-896-2.7	100	16	4/6	C25	1	1000	nil
	PB14-896-2.7	100	14	4/6	C25	1	1000	nil

B is the width of CFRP; d is the diameter of screw rod; n is the number of CFRP layer; ρ is the reinforcement ratio; μ is the prestress level; bond(Yes) represents the CFRP is bonded with concrete.

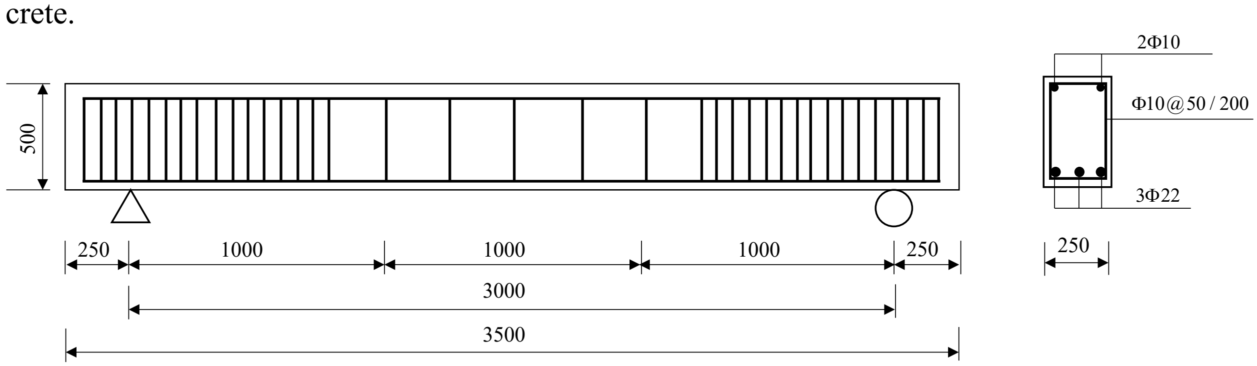

(a) Dimension of RC beams.

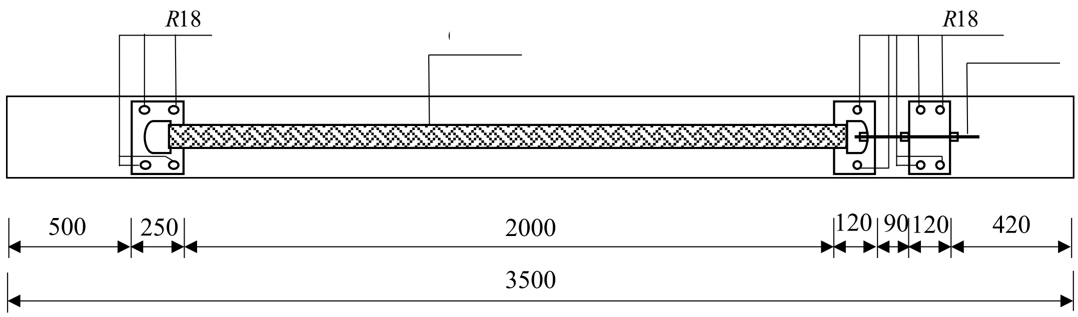

(b) Prestressed CFRP anchorage system.

Figure 3 Dimension and detailing of specimens.

2.1.4 Prestress loss monitoring

The stress loss of prestressed CFRP was monitored for 72 hours to verify the stability of preloading. Specifically, the average stress loss of CFRP were 5.71% for LA-1, 14.30% for LA-2, 7.50% for LA-3, 6.67% for PRB14-896-2.7 and 4.85% for PRB16-896-2.7, respectively. As LA-2 is prestressed with bonded CFRP sheet, it could be seen from Fig. 4 (b) that the bond leads to a higher stress loss rate of prestress. In addition, the initial prestress of other specimens was close to 3500 με with stress loss rate less than 10%, as shown in Fig. 4 (a), (c), (d) and (e). For impact specimens PRB14-896-2.7 and PRB16-896-2.7, the strain development of screw rods was also monitoring which was much lower than that of CFRP. Therefore, the application of prestress on the specimens is stable which indicates the proposed novel H-type end anchor system is adequate.

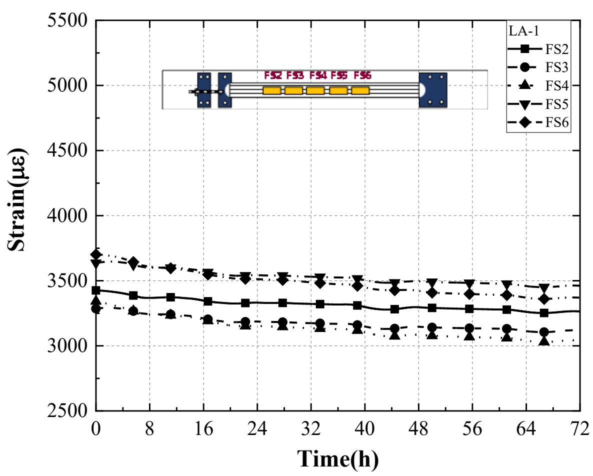

(a) LA-1

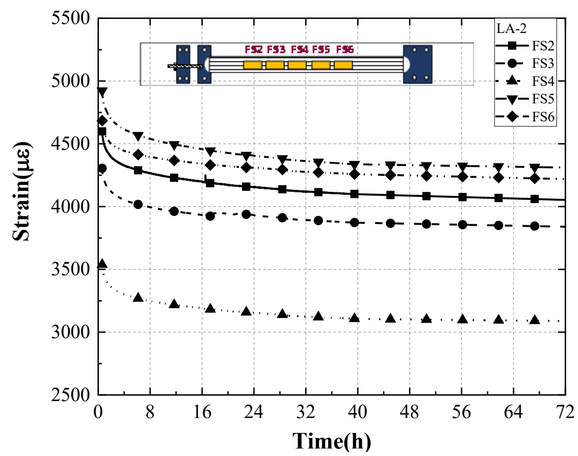

(b)LA-2

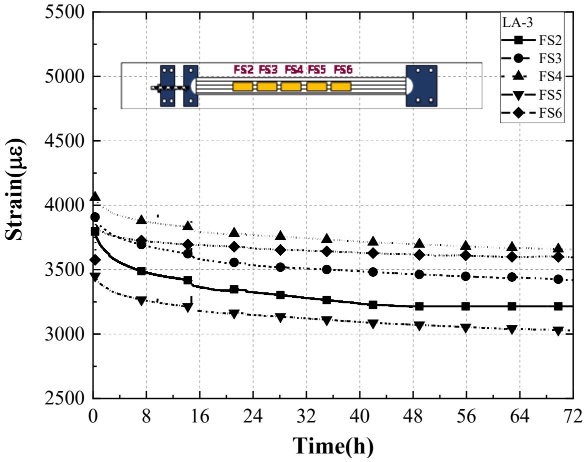

(c) LA-3

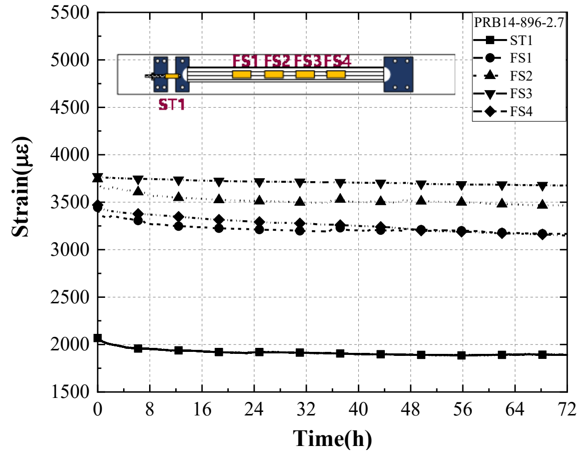

(d) PRB14-896-2.7

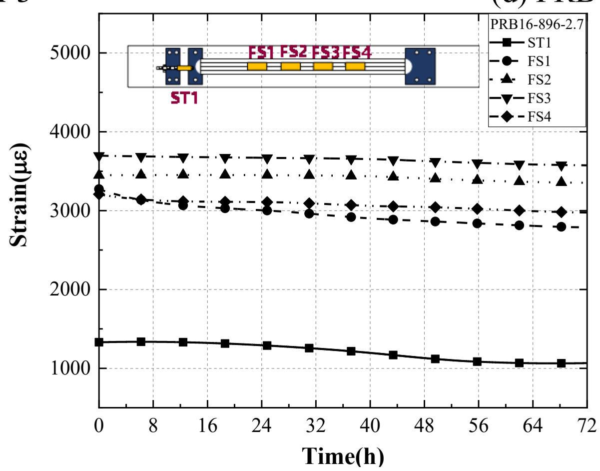

(e) PRB16-896-2.7

Figure 4 Monitoring of prestress loss of CFRP and screw rods.

2.2 Test setup and Instrumentation

Four-point monotonous bending tests under displacement controlled with a loading rate of 0.5mm /min using a 10000 kN hydraulic universal testing machine was carried out. For bending tests, the test variables include prestress level of CFRP, diameter of screw-rod and bond condition, while for impact tests the test variables include screw-rod diameter and impact cycles. The bending region and the shear region of this test were both 1000 mm in length, as shown in Figure 5a and 5b. The displacement sensors were used to measure the mid-span deflection of the beam (i.e., LVDT-1 and LVDT-2), the deflection under the loading point (i.e., LVDT-3 and LVDT-4), respectively. For data collection, the bending test used the Dewsoft dynamic acquisition with frequency of 1 Hz to collect the data of strain, force and displacement.

The impact test setup and instrumentation are shown in Figure 5c and 5d. The maximum weight of the drop hammer is 1 ton with a maximum lifting height of 5 meters. The hammer was dropped from the target height to the mid-span of RC beams and multiple impacts were conducted in the impact tests. Simply supported at both ends were used, and steel tie rods and steel beams were set at the supports to fasten the specimens to prevent rebounding during impact. The history of impact force, strain, displacement and acceleration of the specimen were recorded by the high-speed acquisition data log, while the concrete cracking and failure pattern of each specimen were captured by the high-speed camera. The specific location of the strain gauges, LVDTs and accelerometer are shown in Figure 5c. Table 7 shows the parameters for impact tests.

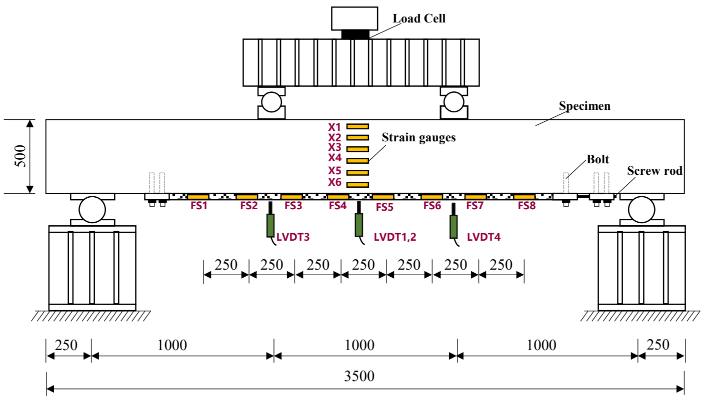

(a) Static four-point bending test setup.

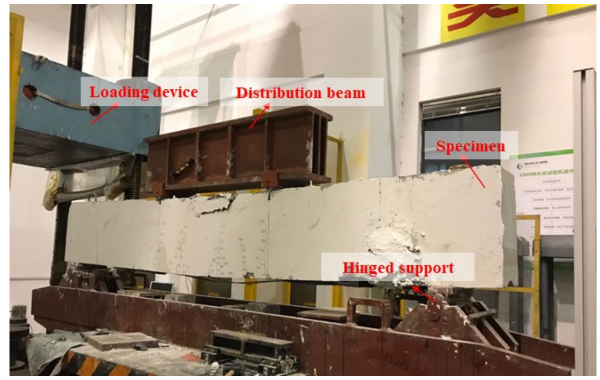

(b) Specimen after bending test.

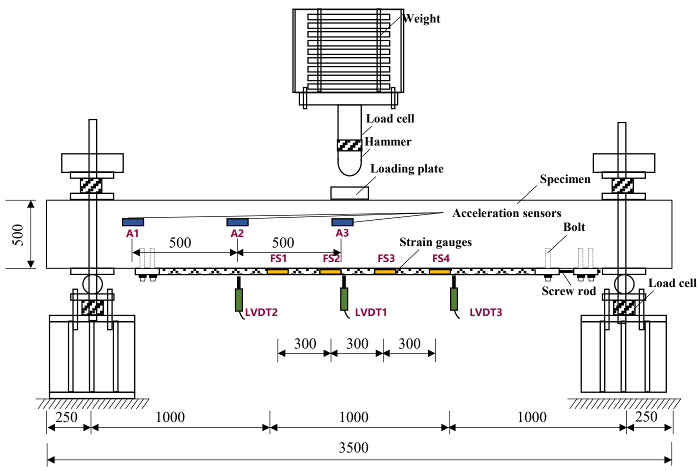

(c) Drop-weight impact test setup.

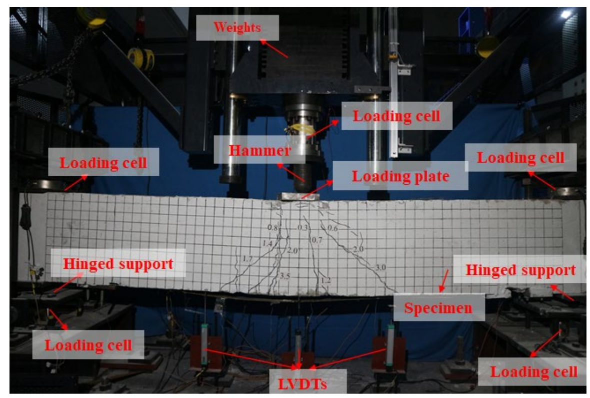

(d) Specimen during impact test.

Figure 5 Test setup and instrumentation.

Table 7 Parameters for impact tests.

Specimen ID	Mass (kg)	Height (m)	v_1 (m/s)	v_2 (m/s)	v_2 / v_1	E_1 (J)	E_2 (J)	E_2 / E_1
NB-896-2.7(1st)	896	2.7	7.28	7.06	97.1%	23730	22355	94.2%
PRB16-896-2.7(1st)	896	2.7	7.28	7.15	98.3%	23730	22928	96.6%
PRB14-896-2.7(1st)	896	2.7	7.28	7.15	98.3%	23730	22928	96.6%
NB-896-2.7(2nd)	896	2.7	7.28	7.07	97.1%	23730	22361	94.3%
PRB16-896-2.7(2nd)	896	2.7	7.28	7.15	98.3%	23730	22928	96.6%
PRB14-896-2.7(2nd)	896	2.7	7.28	7.15	98.3%	23730	22928	96.6%
NB-896-2.7(3rd)	896	2.7	7.28	6.98	95.8%	23730	21827	92.0%

Note: v_1 is calculated by $v_1 = \sqrt{2gh}$, v_2 is measured by the laser velocimeter in the test; E_1 is calculated by $E_1 = 0.5 m v_1^2$ and E_2 is calculated by $E_2 = 0.5 m v_2^2$.

3. Test Results and Discussions

3.1 Static test

3.1.1 Cracking pattern and failure modes

Under four-point bending, the main failure modes of the specimens include (1) typical flexural failure of RC beam (LA-0), (2) fracture of CFRP associated with concrete crushing in compressive region of RC beam (LA-1 and LA-2), and (3) yielding of screw-rod associated with concrete crushing in compressive region of RC beam (LA-3). Generally, all the designed beams fail in a ductile mode. The typical flexural cracks at the bottom and crushing at the compressive region are observed as shown in Figure 6. Specifically, for LA-1, LA-2 and LA-3, the flexural cracks appeared later than LA-0, it is because the prestressed CFRP strengthened RC beams with screw-rod fuse system exhibits good composite action, leading to higher flexural stiffness. As the external load increases, the flexural cracks develop upward with moving up the neutral axis. CFRP sheet in specimens LA-1 and LA-2 has reached the tensile strength and utilized its material strength, thus resulting in a slightly brittle failure. While the screw-rod in LA-3 yields with relative obvious and adequate warning of impending deformation, which is an ideal failure mode for structural design. Therefore, three more full-scale RC beams are finally designed to investigate the impact performance according to the behavior of LA-3.

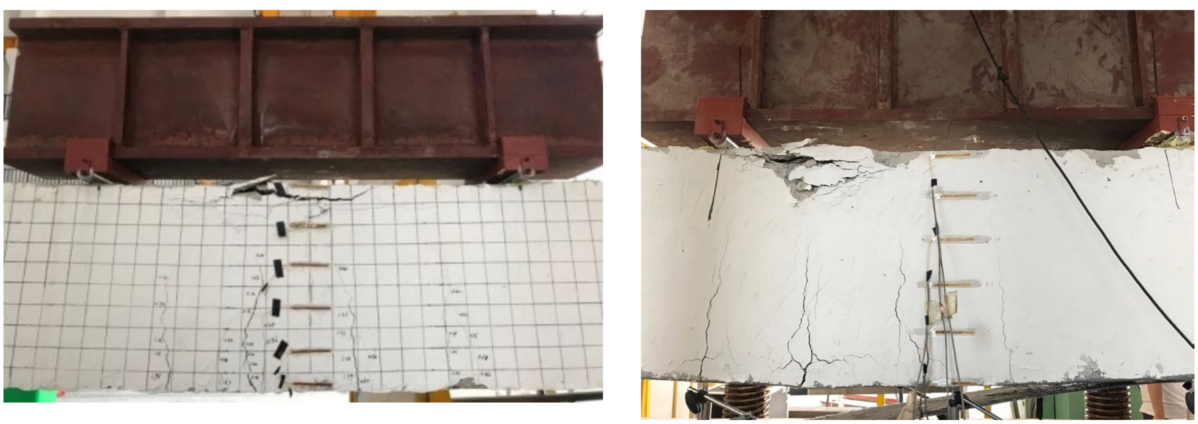

(a) LA-0 (b) LA-1

(c) LA-2 (d) LA-3

Figure 6 Failure modes under static loading

3.1.2 Load-displacement response and ultimate strength

The load-displacement curves of the strengthened RC beams under static loads are presented in Figure 7. Table 7 shows the cracking load (P_{cr}), yield load (P_y) and ultimate load (P_u) and corresponding mid-span displacement of each beam. Based on the failure, three characteristic points divide the whole failure process into four stages: (1) the elastic stage before the cracking load, (2) the elastic-plastic stage after the cracking load, (3) the plastic stage from yield load to peak load, and (4) the residual stage after the peak load. The ultimate load resistance of LA-0, LA-1, LA-2 and LA-3 are close with a difference within 35%, which are 511kN, 555 kN, 610 kN and 690 kN respectively. Specimens LA-1, LA-2 and LA -3 have higher stiffness compared to LA-0, which indicated that CFRP strengthening improves the total section stiffness rather than flexural resistance.

Figure 7(a) show that the strengthening with bonded prestressed CFRP has little influence on the flexural stiffness but lead to higher flexural resistance. Figure 7(b) shows that the flexural resistance of the specimens increases with the increase of the initial prestress of CFRP sheet, as comparing the load displacement curves of LA-1 and LA-3. Suitable design of "fuse" diameter in this anchorage system leads to improve the yield deformation by about 30%, which greatly improves the ductility of the flexural members. According to Table 8, LA-1 and LA-3 exhibit higher ductility index I_D compared to that of LA-0 and LA-2. LA-2 has 38.5% lower ductility index than LA1, probably because of the bonded CFRP which has significant effect on the unloading behavior.

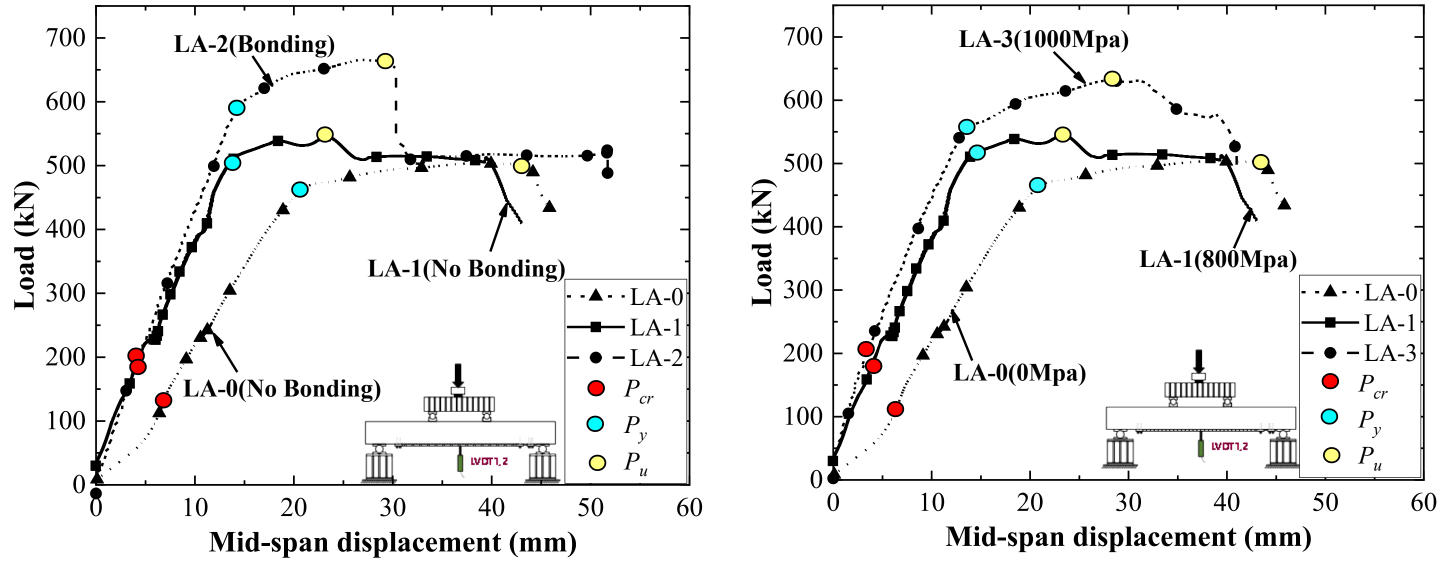

(a) Effect of CFRP bonding (b) Effect of CFRP prestressing strength

Figure 7 Load-displacement curves of RC beams.

Table 8 Summary of characteristic load and deformation.

Specimen	P_{cr} (kN)	δ_{cr}	P_y (kN)	δ_y	P_u (kN)	δ_u	$I_D=\Delta_{0.85}/\Delta_u$
LA-0	125	-	460	-	511	-	1.06
LA-1	196	1.57	526	1.10	555	1.09	1.74
LA-2	200	1.6	614	1.28	690	1.35	1.07
LA-3	206	1.65	562	1.17	640	1.25	1.56

Note: δ_{cr} , δ_y and δ_u are the cracking load factor, yield load factor and ultimate load factor, which equal to the corresponding load ratios of prestressed beam to the reference beam respectively. $\Delta_{0.85}$ and Δ_u are the mid-span displacement corresponding to 85% ultimate flexural resistance during the descending stage and the mid-span displacement at ultimate load P_u, respectively. I_D is the ductility index.

3.1.3 Strain analysis

Figures 8(a-d) shows the development of concrete strain of all RC beams. It can be seen that under different load levels, the strain development of concrete along the section height follows the assumption of plan section remains plan. The neutral axis of specimen with prestressed bonded CFRP has about 10 mm higher than that of the unbonded specimens.

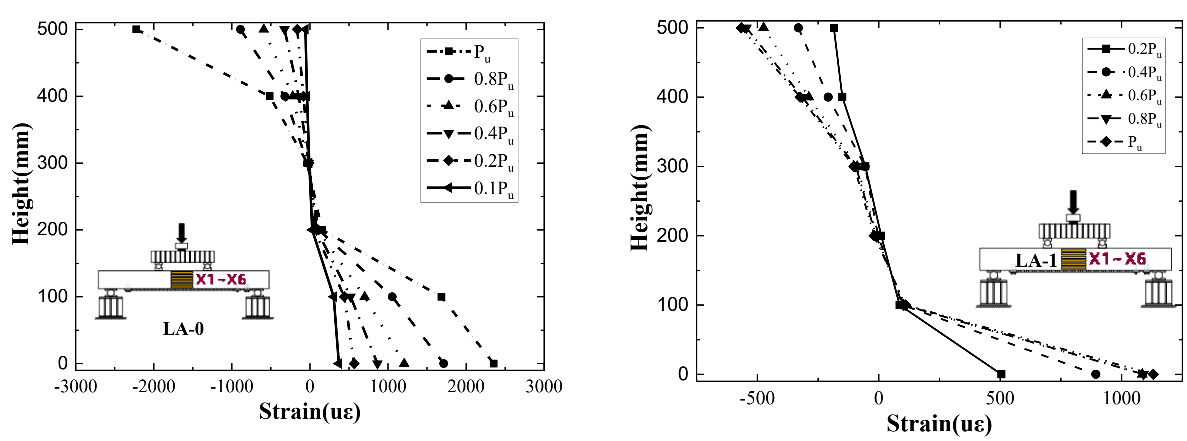

（a）LA-0 （b） LA-1

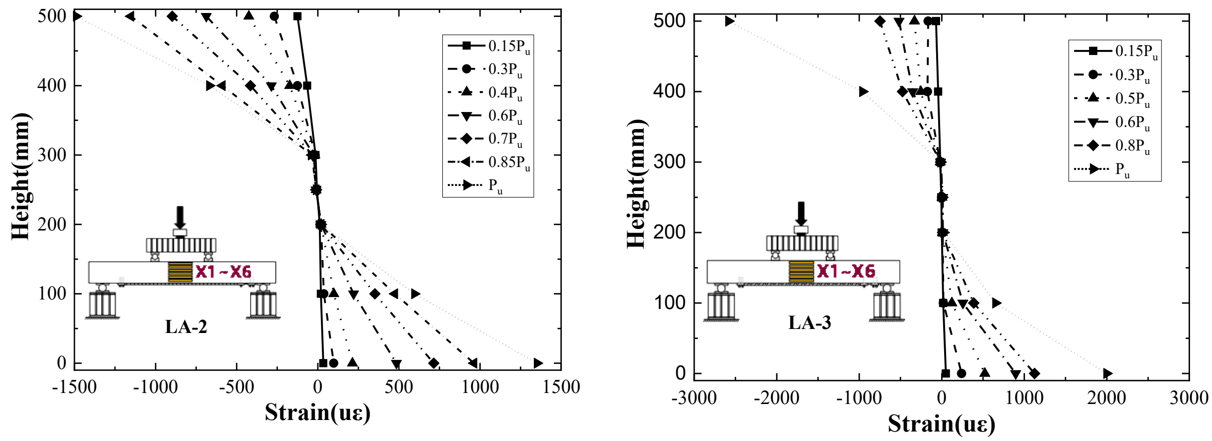

（c） LA-2 （d） LA-3

Figure 8 Concrete strain development and distribution along mid-span cross-section.

Figures 9 show the strain development of longitudinal reinforcement and screw rod. It can be clearly seen that longitudinal reinforcement and screw rod all yield before approaching the peak load, which indicates that the specimen has utilized the material strength. Compared with LA-2 and LA-3, LA-2 that strengthened by bonded CFRP with high prestress level can carry a part of tensile force and LA-3 with smaller screw rod diameter exhibits higher ductility behavior, leading to higher tensile strain development in LA-3 than that of LA-2. Therefore, the ductility index of LA-3 improves 45.8% than that of LA-2. This indicates that the ductility and flexural resistance of prestressed CFRP strengthened RC beams can be improved by appropriate design of screw rod. The proper design of screw rod enables to effectively activate the yielding of screw rod and achieve the function of overload warning.

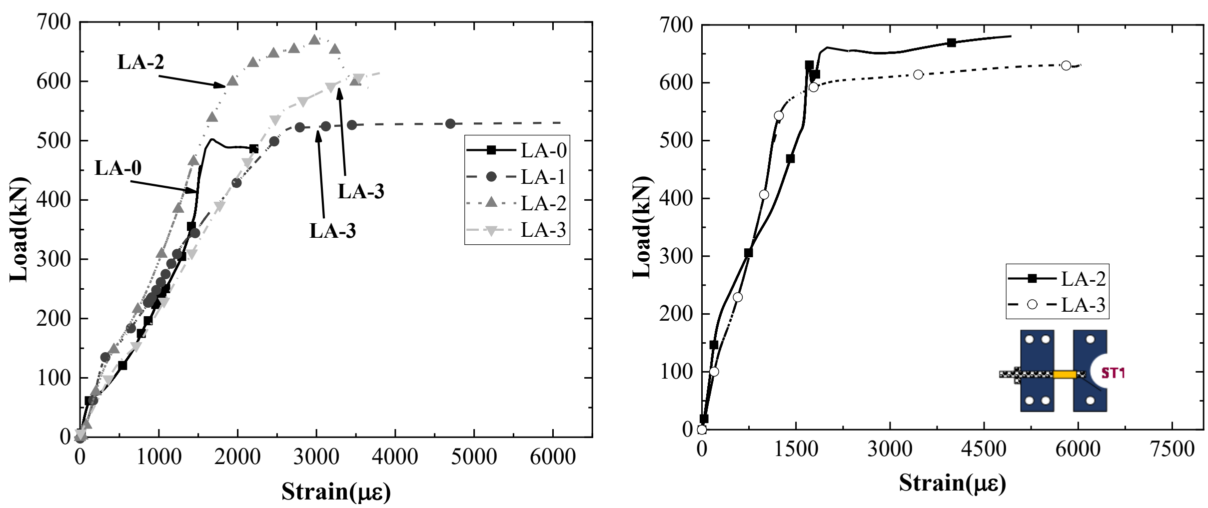

(a) Load-strain of longitudinal reinforcement (b) Load-strain of screw rod

Figure 9 Load-strain of reinforcement and screw rod.

Figure 9 shows the strain development of CFRP under static loading. From Figures 10(a), (c) and (e), the strain of CFRP distributed evenly along the length. Among Figures 10(b), (d) and (f), the strain of CFRP in the mid-span region are higher than that near the beam ends due to the boundary effect. However, as the load increases, the tensile strain of CFRP in LA-2 and LA-3 increases. The CFRP sheet starts to fail when the tensile strength approaches to around 6000~8000 με.

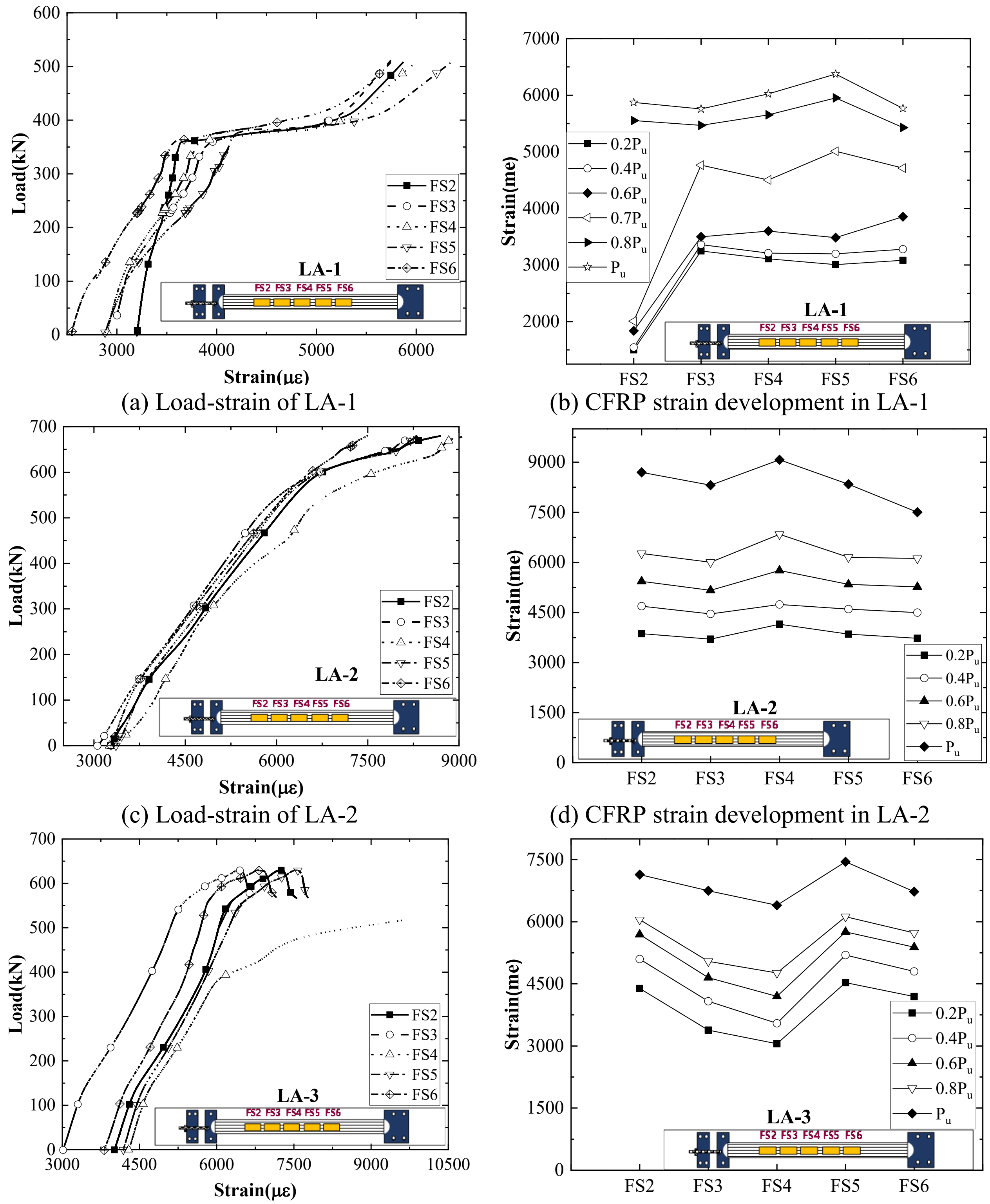

(a) Load-strain of LA-1 (b) CFRP strain development in LA-1

(c) Load-strain of LA-2 (d) CFRP strain development in LA-2

(e) Load-strain of CFRP-LA-3 (f) CFRP strain development in LA-3

Figure 10 Load-strain of CFRP in specimens.

3.2 Impact test

3.2.1 Failure mechanism

Figure 11 shows the failure mode of each specimen after impact. All the specimens failed by flexural mode under first impact associated with local crushing of concrete at the impact region. The crack number and width are highlighted in the figure. Most of the concrete cracks are mainly distributed radially from the impact point to the bottom (around 45°). The crack width is larger at the bottom part of the mis-span than that at the impact point in which crack width is generally less than 1mm, as shown in Figure 11. Under similar impact energy, the impact area of PRB14-896-2.7 exhibits relatively less damage than NB-896-2.7 and PRB16-896-2.7 in which the concrete of the impact area is seriously damaged associated with greater crack depth and more crack paths. The screw rod of PRB14-896-2.7 and PRB16-896-2.7 yield under the first impact with the CFRP fracture near the anchorage section. The ductile yielding failure of screw rod plays a certain warning function in the test.

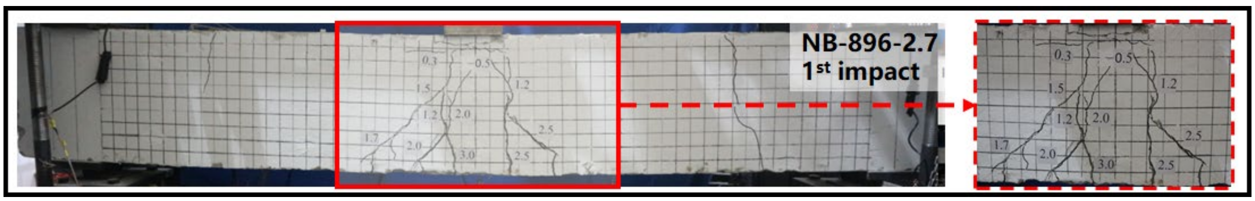

(a) NB-896-2.7

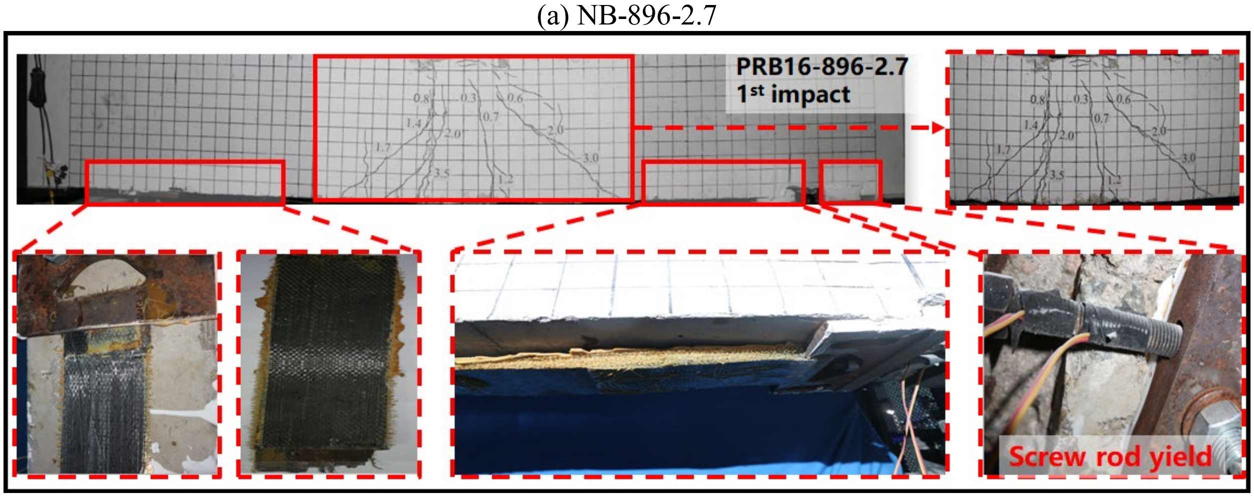

(b) PRB14-896-2.7

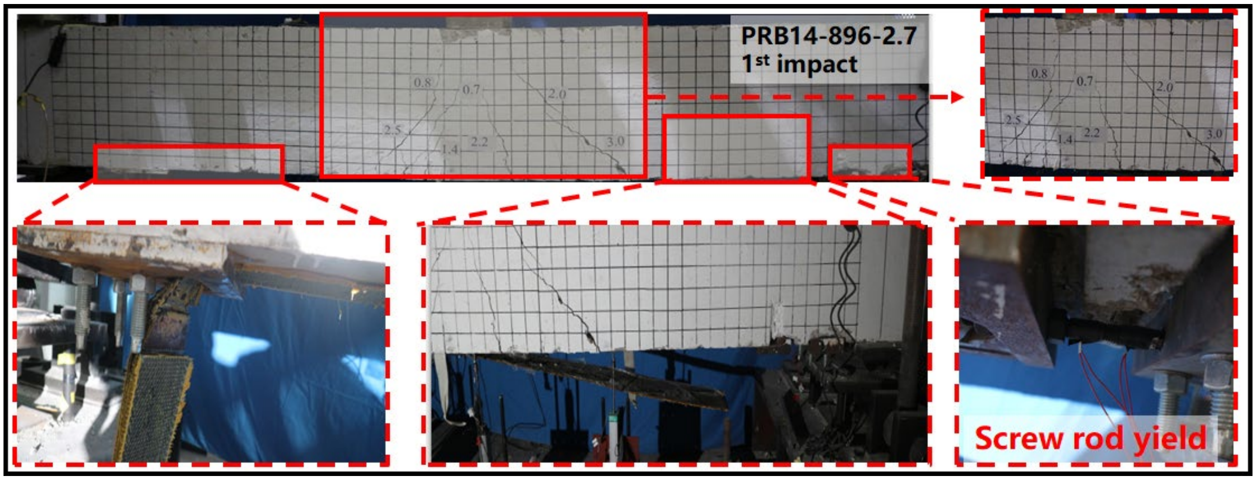

(c) PRB14-896-2.7

Figure 11 Failure modes of the beams subjected to first impact

Figures 12a-12c show the typical period of crack development recorded by high-speed camera under impact loading, which respectively include the moment of (1) peak impact force (1ms); (2) crack initiation; (3) peak displacement (18ms) and (4) hammer rebound point (25ms). Specifically, as shown in Figure 12a, NB-896-2.7 reaches the peak impact force at 1ms after impact. Micro-cracks along an inclination angle of 45° developed from the bottom to the top of the beam. The contact area between the drop hammer and the concrete remains intact. After 3ms, the vertical crack width at the mid-span increases gradually with the number of propagation path increases to the top of the beam. When approaching the peak displacement (18ms), the crack has propagated completely along the path. The hammer rebound occurs as the energy is absorbed and later released. The concrete crack development process experiences initiation, spreading, extension, expansion and finally closure. As shown in Figures12b and 12c, PRB16-896-2.7 and PRB14-896-2.7 show similar failure modes to NB-896-2.7, but with less flexural crack and relatively smaller crack opening. From the above discussion, it can be concluded that: (1) compared with ordinary RC beams, prestressed CFRP RC beams tend to deepen the crack width and produce fewer cracks in the process of crack development; (2) the cracks appear later in the prestressed CFRP strengthened RC beams than ordinary RC beams, which is due to the prestress effect of CFRP on concrete that improves the flexural stiffness of beams.

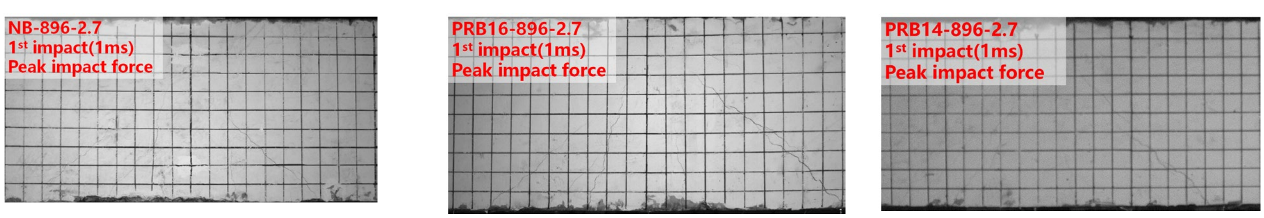

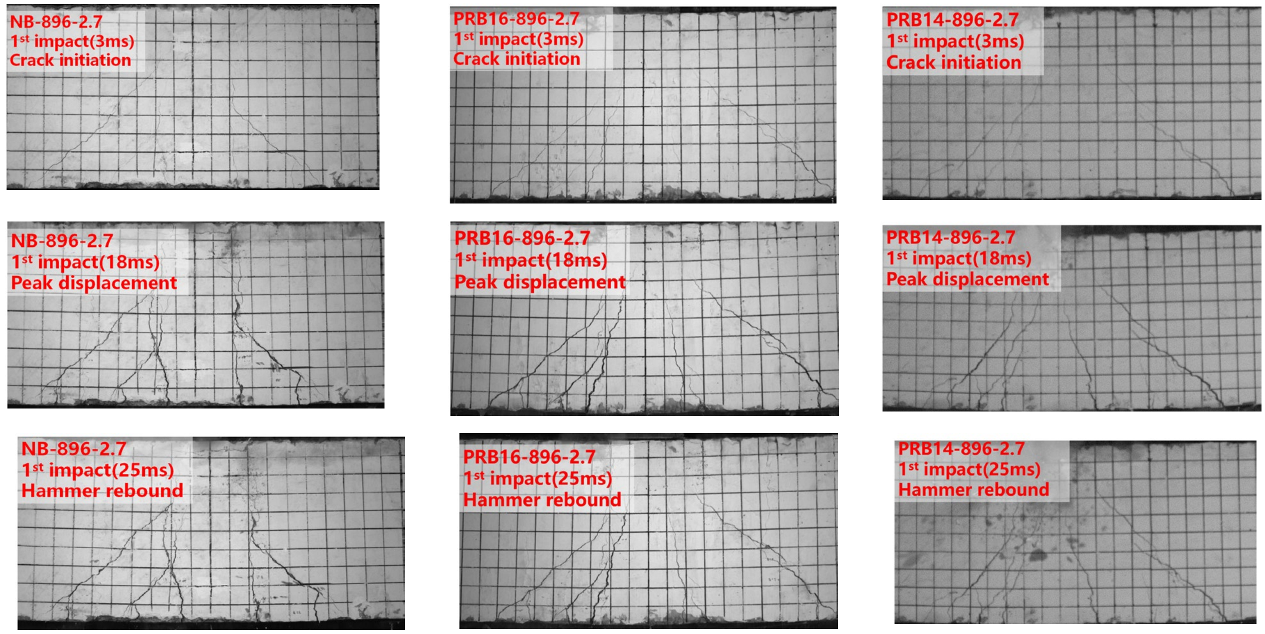

(a) Crack propagations of NB-896-2.7 (b) Crack propagations of PRB16-896-2.7 (c) Crack propagations of PRB14-896-2.7

Figure 12 Crack propagations of RC beam subjected to single impact

3.2.2 Dynamic response

Figures 13a-13h show the time-history curves of impact force, reaction force, inertia force and midspan displacement, in which the reaction force equals to the sum of two support reactions. The impact force history is mainly composed of four sinusoidal half waves. The first temporary wave has a short duration with a peak value, but rapidly decays to zero within 3ms. However, the duration of the subsequent main wave was longer and the peak value decays within a relative longer time period. Although the strengthening conditions of the three beams are different, the impact force history is similar. The peak impact force of NB-896-2.7, PRB16-896-2.7 and PRB14-896-2.7 are 1653.53kN, 1610kN and 1702.14kN respectively, as shown in Figure 13g. At the early stage of the impact force history, there was an obvious difference between the impact force and the reaction force, and then the main wave shape of the impact force was almost the same as the reaction force curve, which indicated that the inertial force played a significant role in the initial stage of impact, as shown in Figure13b,13d and 13f.

Figures 13a, 13c and 13e show the midspan displacement history curves of specimens under first impact. The maximum midspan displacement of NB-896-2.7, PRB16-896-2.7 and PRB14-896-2.7 are 47.55mm, 47.31mm and 44.45mm, respectively. The maximum midspan displacement of PRB14-896-2.7 was less than that of NB-896-2.7 after strengthening with prestressed CFRP. The time period required for PRB14-896-2.7 to reach the peak deflection becomes shorter.

As shown in Figures 13a, 13c and 13e, tensile force has been detected in the initial stage of impact on the reaction force history curves, and then the waveform gradually coincides with the main wave of the impact force history curve. The tensile force was measured by the pressure gauge that placed on the top and bottom of the supports. Due to the lag effect of stress wave transmission at the concrete interface, the reaction force does not react immediately with the impact force.

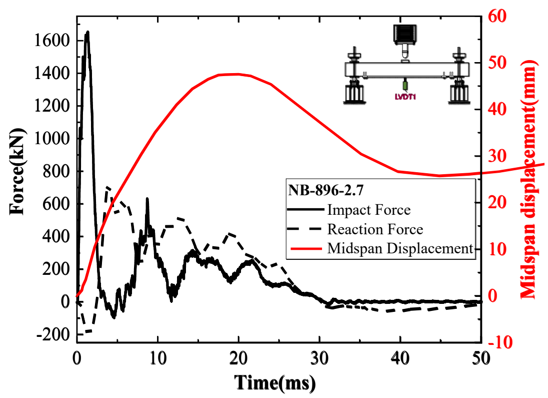

(a) Impact force, reaction force and displacement curve of NB-896-2.7

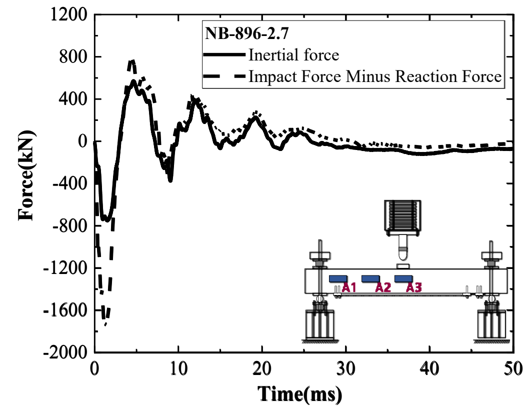

(b) Inertial force curve of NB-896-2.7

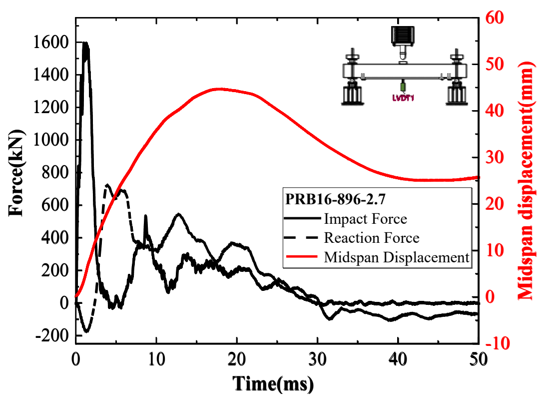

(c Impact force, reaction force and displacement curve of PRB16-896-2.7

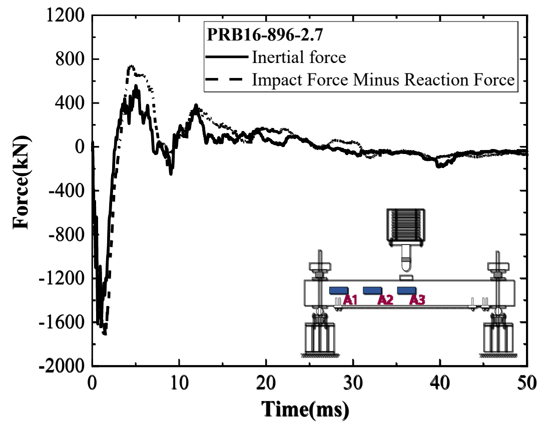

(d) Inertial force curve of PRB16-896-2.7

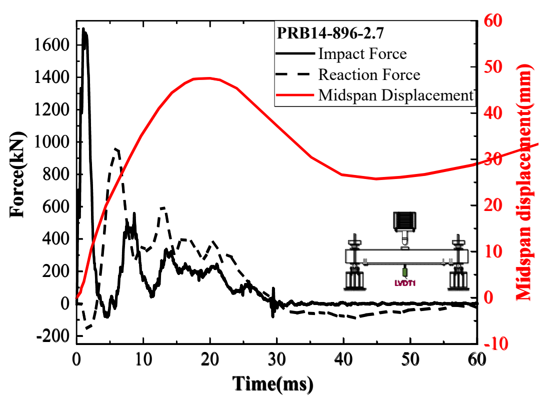

(e) Impact force, reaction force and displacement curve of PRB14-896-2.7

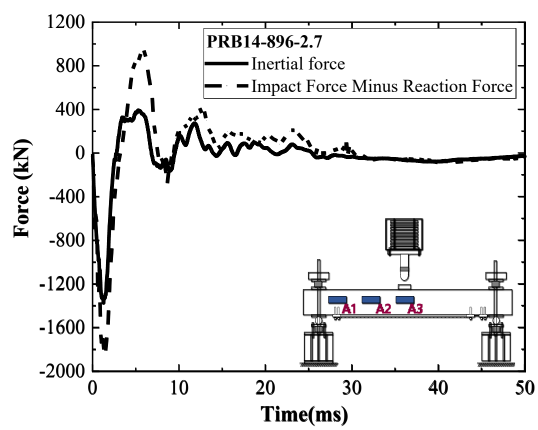

(f) Inertial force curve of PRB14-896-2.7

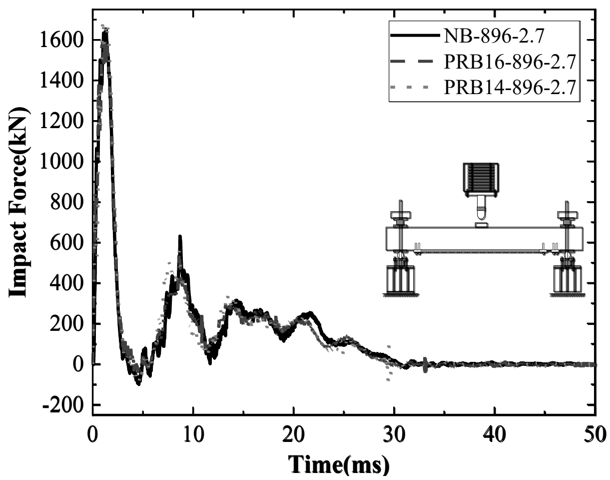

(g) Comparison of impact force history

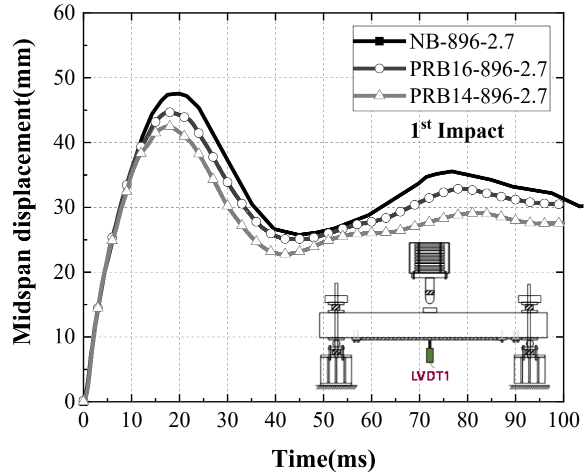

(h) Comparison of midspan displacement history

Figure 13 Impact force, reaction force and displacement history

According to Newton's second law, the inertial force is equal to the value of mass multiplied by the acceleration. The inertial force of the test beam can be calculated based on Eq.(1) ,

$$\int_0^l \overline{m}\ddot{u}(x,t)\,dx = \overline{m}L_1\left[a_1(t)+a_2(t)\times 2+\frac{3}{4}a_3(t)\right] \qquad (1)$$

where $\overline{m}$ is the mass of the RC beam per unit length; L_1 is the spacing of accelerometers (0.5m); $a_i(t)$ is the acceleration history captured by the accelerometer *i*.

Figure 14 shows the distribution of acceleration at point A1, A2 and A3 along the beam length of the specimens (*t*=1ms) under first impact. Considering the existence of cantilever part of the test beam with length of 250mm, the peak value at both ends is selected as A1/2, while the peak value at the support is set to 0 [16].

According to d 'Alembert's principle, inertial force is equal to impact force minus reaction force. The accuracy of the measurement of inertial force in this test can be verified by the principle. As shown in Figure 13 (c), the inertial force history measured agrees well with the impact force minus the reaction force obtained in the support, thus verifying the reliability of the impact test. Figures 14a-14c show the peak acceleration in the mid-span area, in which the mid-span peak acceleration of the CFRP prestressed beam is 15% lower than that of the RC beam.

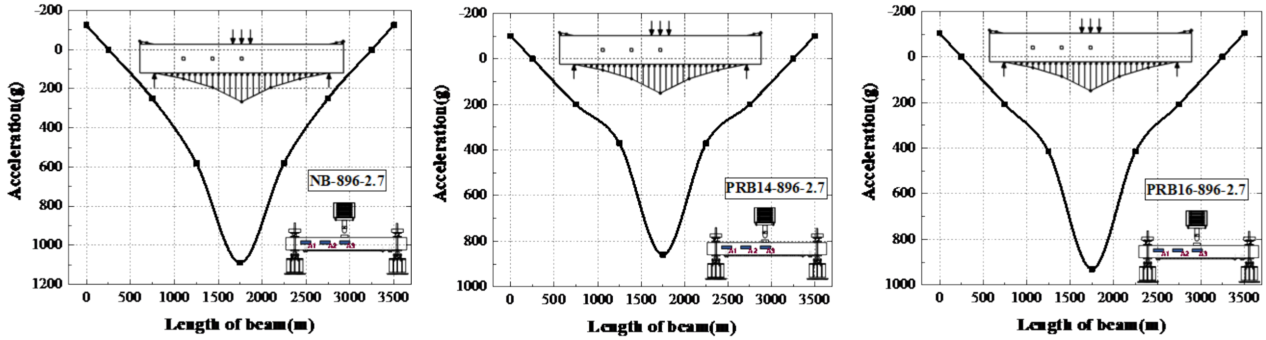

(b)NB-896-2.7 (b)PRB14-896-2.7 (c)PRB16-896-2.7

Figure 14 Acceleration distribution along the beam length.

3.2.3 Strain development of rebar, CFRP and screw rod

Figures 15a-15d show the strain histories of the flexural reinforcement, screw rod and CFRP of each beam. Figure 15a shows that the flexural reinforcement strain of each beam reach yield strain at 1ms and then fluctuate. Unlike NB-896-2.7, PRB14-896-2.7 and PRB16-896-2.7 experience peak strain and then maintain a certain level of residual strain. While for NB-896-2.7, the strain of flexural reinforcement dramatically drops to zero after peak strain. Figure 15b shows the strain development history of screw rod. The yield strain of screw rod was activated at 5ms, which indicates that the stress wave propagates longitudinally along the beam. The screw rod strain of PRB14-896-2.7 and PRB16-896-2.7 shown in Figure 15b approaches to around 3000με which is similar to that of CFRP when CFRP breaks. Figure 15c and 15d show the CFRP strain of PRB14-896-2.7 and PRB16-896-2.7. Specifically, the strains of FS2 and FS3 near the mid-span were higher than that of FS1 and FS4. The flexural crack of PRB14-896-2.7 extended from the mid-span near FS3 and FS4, thus the strains of FS3 and FS4 were almost the same. Correspondingly, FS2 has the highest strain value among the strain gauges, increasing to about 3500με before CFRP breaks. This indicates that the hybrid system exhibits good composite action to resist the impact load. Liu and Xiao [17] mentioned that the strain rate obtained by dividing the peak strain in the initial increasing stage by the corresponding time interval is regarded as the average strain rate of CFRP. Thus, the average strain rate of PRB14-896-2.7 and PRB16-896-2.7 is about $2.4s^{-1}$ and $1.7s^{-1}$, respectively. Al-Zubaidy et al.[18] found that when the strain rate is less than $10s^{-1}$, the dynamic tensile strength and elastic modulus of CFRP increased by only about 3%. Therefore, the effect of strain rate on the CFRP in PRB14-896-2.7 and PRB16-896-2.7 may not be significant in the current impact test.

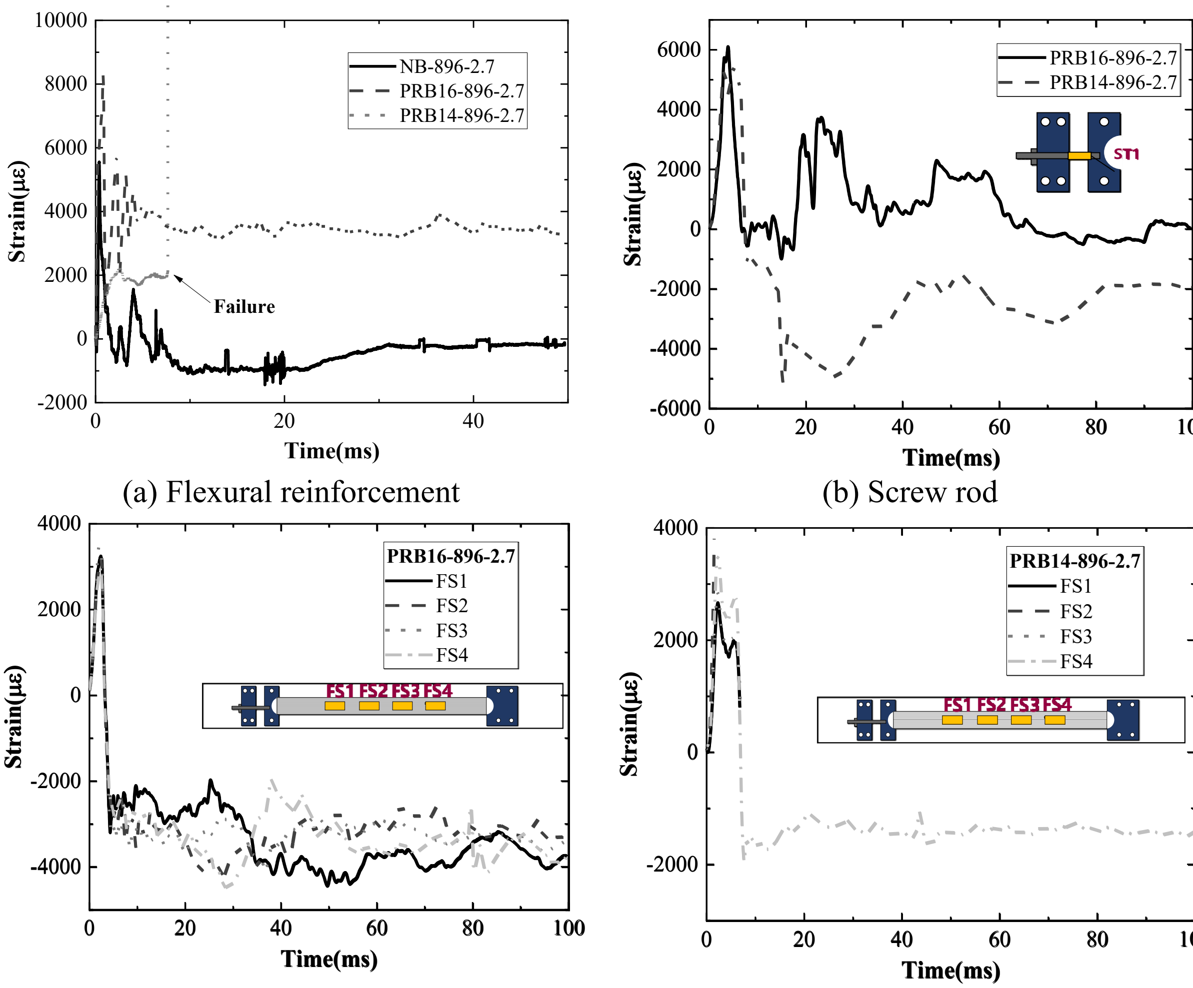

(a) Flexural reinforcement (b) Screw rod

(c) CFRP in PRB16-896-2.7 (d) CFRP in PRB14-896-2.7

Figure 15 Dynamic strain development of reinforcement, screw rod and CFRP.

3.3 Multi-impact test

3.3.1 Failure mechanism

NB-896-2.7 has experienced three consecutive impacts with the same energy. At the 1st impact, the specimen subjected to flexural failure. After the 2rd impact, the number of cracks in the specimen did not increase significantly, but the crack width enlarged associated with concrete significantly crushed at the impact area. The mid-span deflection further increased. After the 3th impact, the concrete at the impact area is fully crushed, and the whole specimen body loses its carrying capacity and collapses, leading to the exposure of the longitudinal rebar and stirrups in the bending area, accompanied with pronounced residual deformation, as shown in Figure 16 (a-b).

PRB14-896-2.7 and PRB16-896-2.7 experienced two consecutive equal-energy impact. The second impact caused to produce an diagonal crack with angle of about 45° down from the loading point. The concrete at the impact area was crushed, but the beam body remained intact, and the crack width was smaller than that of that in NB-896-2.7. After the first two impacts, the specimens have flexural cracks appeared and thus accumulated a certain level of damage, while the CFRP strengthening has failed.

Figure 17 shows crack propagations of PRB14-896-2.7 and PRB16-896-2.7 subjected to 2nd impact loading. The number of flexural cracks increased in the mid-span in PRB16-896-2.7 after the second impact. Comparing PRB14-896-2.7 with PRB16-896-2.7, it can be seen that smaller diameter of screw rod (14mm) improves the flexural ductility through steel yielding. The failure pattern shows that the crack number and crack width of PRB14-896-2.7 are much less than that of PRB16-896-2.7 under 2nd impact, as shown in Figure 17a and 17b. This indicates that the reasonable design of screw rod can effectively control the damage level of the specimen and has a positive effect on improving the impact resistance.

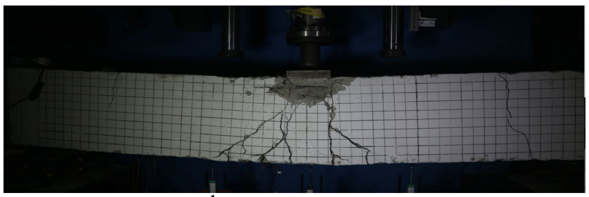

(a) 2nd impact of NB-896-2.7

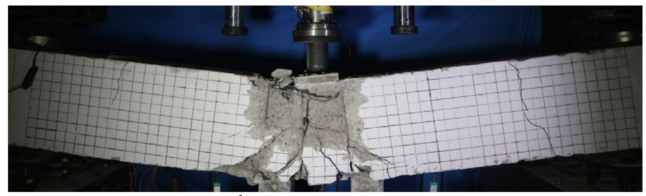

(b) 3rd impact of NB-896-2.7

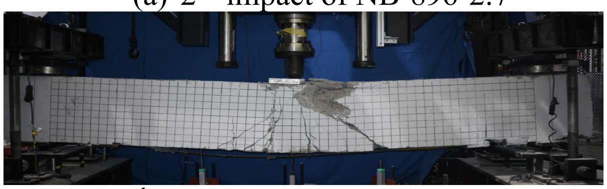

(c) 2nd impact of PRB16-896-2.7

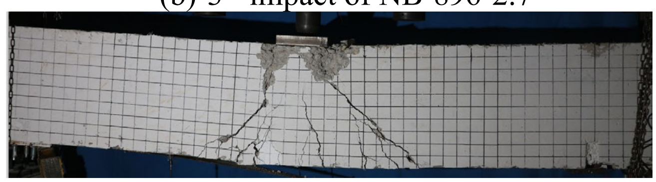

(d) 2nd impact of PRB14-896-2.7

Figure 16 Failure modes under 2nd impact loading.

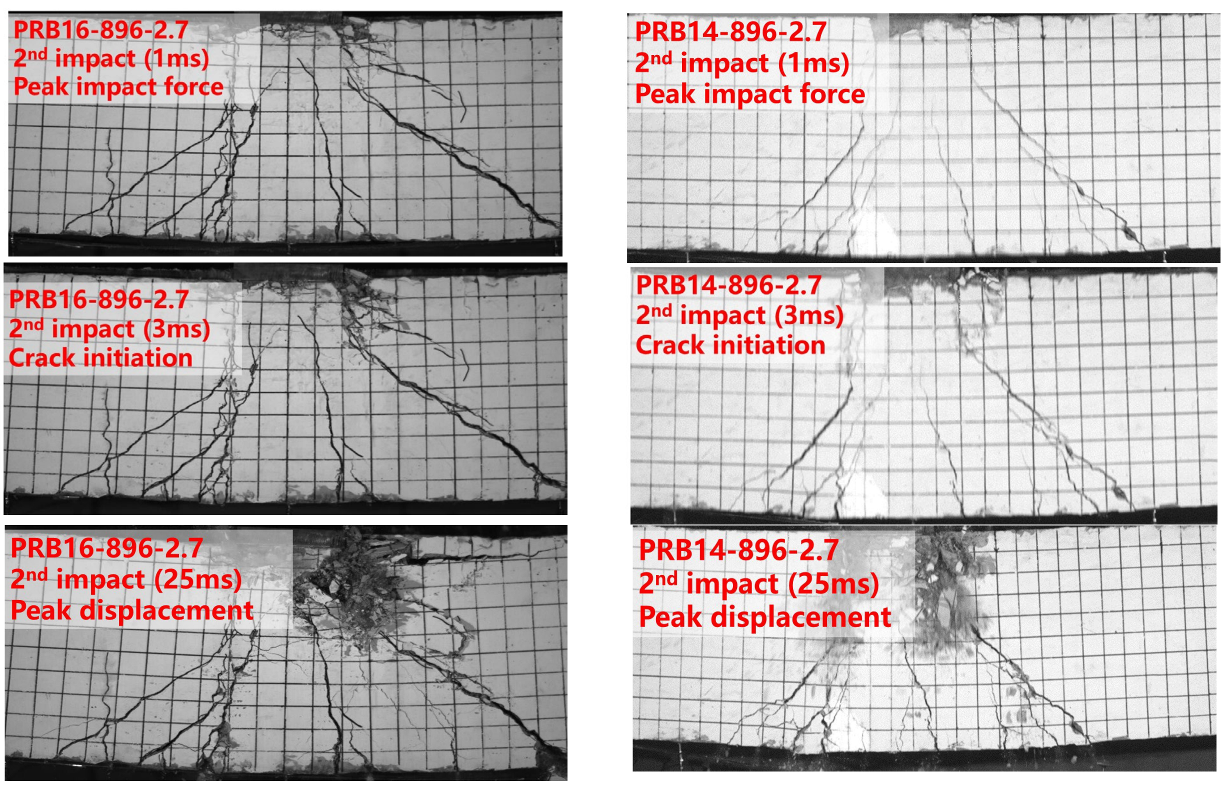

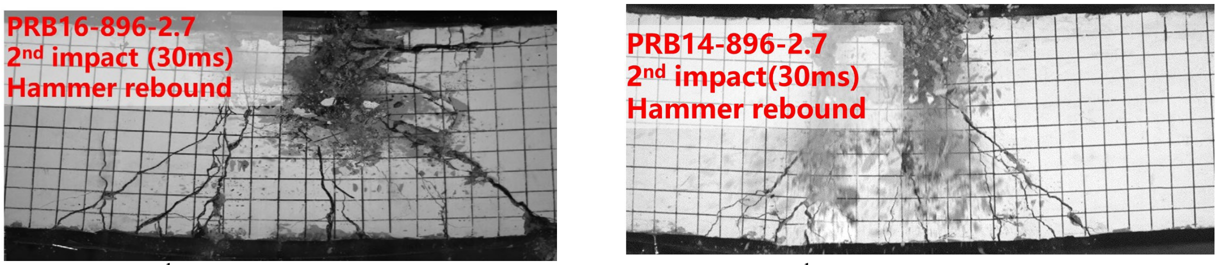

(a) 2nd impact of PRB16-896-2.7 (b) 2nd impact of PRB14-896-2.7

Figure 17 Crack propagations of beams subject to 2nd impact loading.

3.3.2 Dynamic response under multi-impact

Figures 18a and 18b show the impact force history and midspan displacement history of the full-scale specimens under multiple impacts. Taking NB-896-2.7 as an example, for each repeated impacts with the same energy of 23730J, a triangular-form wave appears at the initial stage of the impact force history curve. The first peak force decreases with the increase of the impact cycles. This is because the stiffness of the specimen decreases after cracks appear while the duration of the later dynamic response increases.

The mid-span displacement history curves of PRB14-896-2.7 and PRB16-896-2.7 were similar under the first two impacts, showing that the peak and residual displacements were relatively close. The peak displacement of NB-896-2.7, PRB14-896-2.7 and PRB14-896-2.7 increased by 11%, 23% and 24%, respectively, compared to the first impact. Taking PRB14-896-2.7 as an example, the prestressed CFRP improves the dynamic flexural stiffness to a certain extent, but the amplitude of improvement is not as high as that under the static loading (up to 150%). Under the second impact, the specimen still maintains good integrity. However, under the third impact, the mid-span displacement of NB-896-2.7 dramatically increased and collapsed, which was because the specimens have accumulated a certain level damage after the first two impacts, thus weakening their residual impact performance.

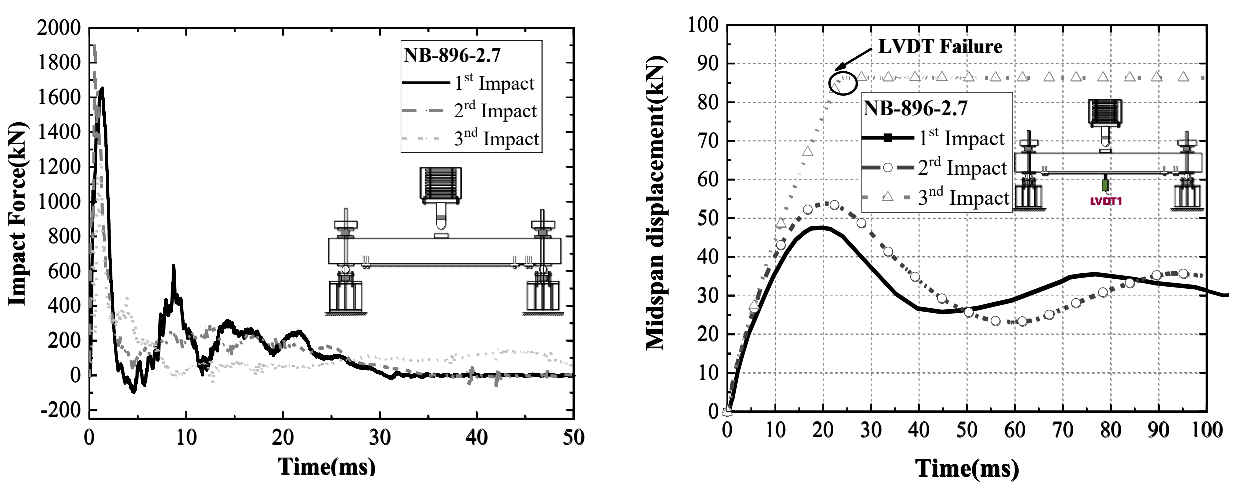

(a)Impact force of NB-896-2.7 (b)Mid-span displacement of NB-896-2.7

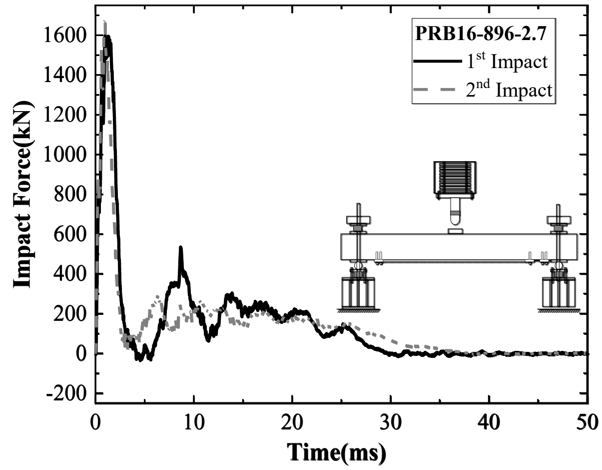

(c)Impact force of PRB16-896-2.7

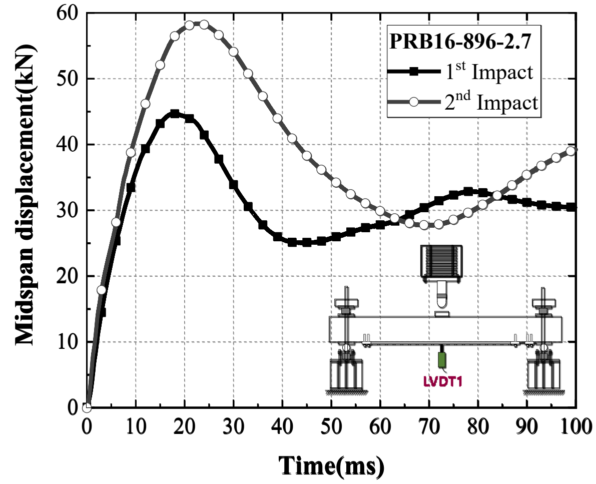

(d)Mid-span displacement of PRB16-896-2.7

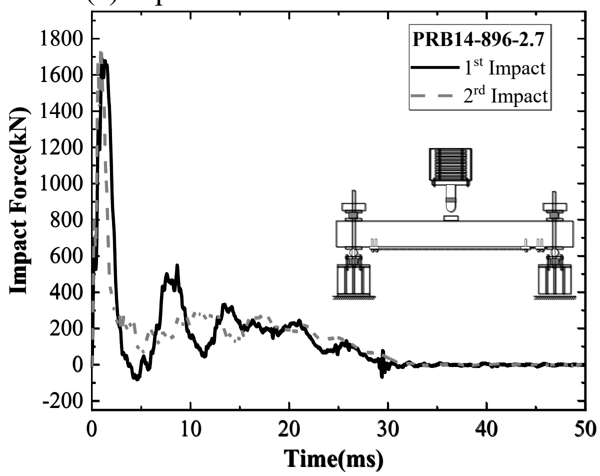

(e)Impact force of PRB14-896-2.7

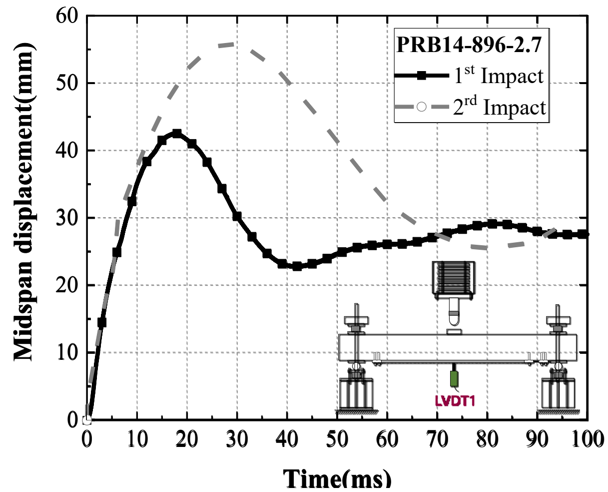

(f)Mid-span displacement of PRB14-896-2.7

Figure 18 Dynamic responses of RC beams under multi-impact.

4. Numerical Investigation

This section applies LS-DYNA to develop a detailed FE model to simulate multi-impact on the prestressed CFRP-strengthened RC beam and normal RC beam as well as validating the dynamic responses. This section also summerizes the simulation methods of multi-impact. Due to symmetry of geometry condition, 1/4 model was established for NB-896-2.7 while 1/2 model was for PRB16-896-2.7 and PRB14-896-2.7 to save computing resources. Figure 19 shows the numerical model of a typical CFRP strengthened RC beam. A three-dimensional eight node hexahedral solid element SOLID164 was used to model the concrete, hammer, loading plate and support. The element adopts constant stress element scheme with single point Gauss integration method which supports material and geometric nonlinearity. BEAM161 was used to model the longitudinal rebar and stirrups. CFRP was modeled by a 2D four node quadrilateral shell element, which adopts the Belyschko-Tsay element scheme with single point integration method along the in-plane thickness direction [19].

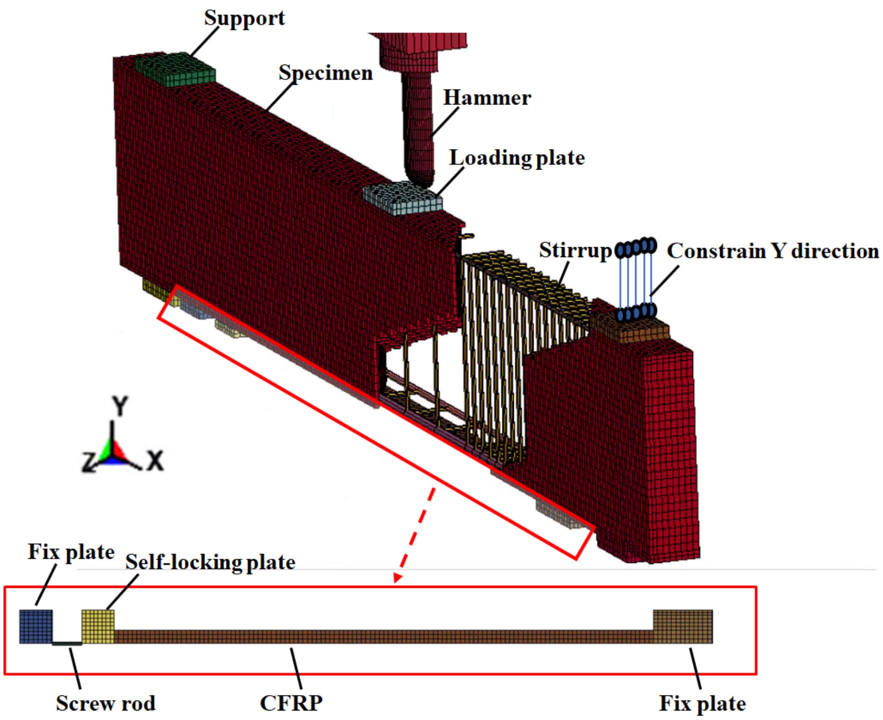

Figure 19 Detailed FE model

4.1 Constitutive model

4.1.1 Concrete

Continuous Surface Cap Model (CSCM) MAT_159 is used to simulate the dynamic behavior of concrete under impact load. MAT_159 is able to represent the strain softening of concrete under low confining pressure and tensile stress. A smooth connection transition is incorporated between the shear failure surface and hardened cap surface, of which eliminates the numerical stability and convergence problem caused by discontinuity. Figure 20 shows the constitutive relation of CSCM concrete models.

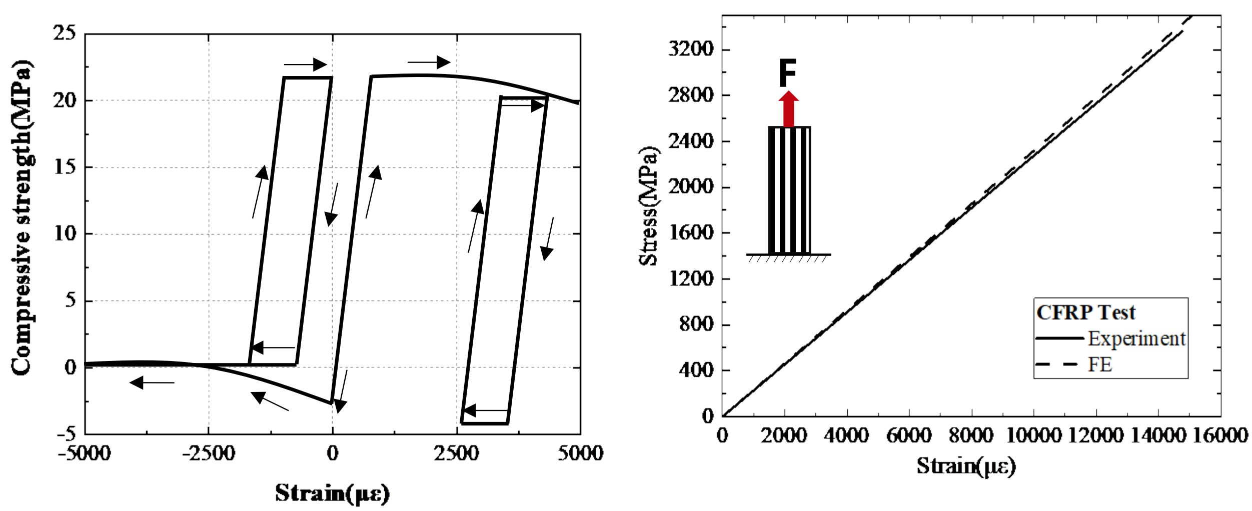

(a) Concrete (b) CFRP

Figure 20 Material models for concrete and CFRP.

4.1.2 CFRP

To accurately predict the behavior of prestressed CFRP, a damaged model MAT_COMPOSITE_DAMAGE (MAT_22) was selected which was based on the Chang-Chang failure criteria [20]. Based on the plane stress status, the linear elastic behavior and brittle failure of composite materials can be characterized by the three failure criteria, as shown in Eqs.(2-4).

(1) Crack failure of CFRP adhesive matrix,

$$F_{matrix} = \left(\frac{\sigma_2}{S_2}\right)^2 + \bar{\tau} \tag{2}$$

If $F_{matrix} > 1$, the adhesive matrix fails by crack. The material parameters E_1, G_{12}, v_1 and v_2 are equal to zero.

(2) Compression failure of CFRP follows Eq.(7),

$$F_{comp} = \left(\frac{\sigma_2}{2S_{12}}\right)^2 + \left[\left(\frac{C_2}{2S_{12}}\right)^2 - 1\right]\frac{\sigma_2}{C_2} + \bar{\tau} \tag{3}$$

If $F_{matrix} > 1$, the fiber fails by compression. The material parameters E_2, v_1 and v_2 are equal to zero.

(3) Fracture of CFRP,

$$F_{fiber} = \left(\frac{\sigma_1}{S_1}\right)^2 + \bar{\tau} \tag{4}$$

If $F_{matrix} > 1$, the fiber fails by fracture. The material parameters E_1, E_2, G_{12}, v_1 and v_2 are equal to zero.

The failure criteria can be achieved by setting five parameters, which are tensile strength S_1 in the fiber direction (longitudinal), tensile strength S_2 in the vertical fiber direction (transverse), shear strength S_{12}, transverse compressive strength C_2 and nonlinear shear stress coefficient α. S_1, S_2, S_{12} and C_2 are determined from the material test of CFRP, while α is calculated by Eqs. (5-8).

$$2\varepsilon_{12} = \frac{1}{G_{12}}\tau_{12} + \alpha\tau_{12}^3 \tag{5}$$

$$\varepsilon_1 = \frac{1}{E_1}(\sigma_1 - v_1\sigma_2) \tag{6}$$

$$\varepsilon_2 = \frac{1}{E_2}(\sigma_2 - v_2\sigma_1) \tag{7}$$

$$\bar{\tau} = \frac{\dfrac{\tau_{12}^2}{2G_{12}} + \dfrac{3}{4}\alpha\tau_{12}^4}{\dfrac{S_{12}^2}{2G_{12}} + \dfrac{3}{4}\alpha S_{12}^4} \tag{8}$$

in which, ε_1 is longitudinal tensile strain; σ_1 is longitudinal tensile stress; E_1 is longitudinal tensile modulus; v_1 is transverse Poisson ratio; ε_2 is transverse tensile strain; σ_2 is transverse tensile stress; E_2 is transverse tensile modulus; v_2 is longitudinal Poisson ratio; ε_{12} is shear strain; τ_{12} is shear stress; G_{12} is shear modulus; $\overline{\tau}$ is shear stress to shear strength ratio.

The CFRP used in this test is mainly governed by the fracture failure of the fiber in longitudinal direction. Therefore, the fiber fracture failure criterion can be characterized by inputting the longitudinal tensile strength $S_1(X_t)$ into the model. The left parameters can use default value. According to Section 3.2.3, the strain rate of CFRP under drop weight impact is less than $10s^{-1}$. Within this range, the increasing ratio of tensile strength and elastic modulus of CFRP is within 3%. Therefore, the strain rate effect of CFRP was ignored [18]. Figure 20b shows the material models of CFRP.

4.1.2 Steel Bar and Screw rod

A piecewise linear elastoplastic model *MAT_PIECEWISE_LINEAR_PLASTICITY (MAT_024) is used to model the dynamic behavior of longitudinal rebar, stirrups and screw rod under impact load. The strain rate effect and hardening effect can both be considered in this model. The modulus of the hardening part uses 1% of the elastic modulus. The enhancement of dynamic yield strength and ultimate strength due to strain rate effect was considered using Cowper-Symonds model, in which the enhancement parameters C and P are set to 40.4 and 5[21], respectively. Rigid body model *MAT_RIGID (MAT_020) was used for the impact plate, while elastic material model *MAT_ELASTIC (MAT_01) was used for the drop hammer and support plates. Table 9 shows the materials properties of each part for the specimens.

Table 9 Material parameters in numerical model

Part	Material model	Parameters
Drop hammer	*MAT_ELASTIC	ρ=7850kg/m³, E=200GPa, ν=0.27
Support plate	*MAT_ELASTIC	ρ=7850kg/m³, E=200GPa, ν=0.27
Concrete	*MAT_CSCM_CONCRETE	ρ= 2400kg/m³, E=30GPa, ν=0.27 f_c=22.7MPa, ERO=1.6, $AgS_{\max}$=30mm
CFRP	*MAT_COMPOSITE_DAMAGE	E_a=230GPa, E_b= E_c =2.3GPa, X_t=3300MPa, Y_t =Y_c= 0, AOPT=2, v_{ab} =v_{bc}= v_{ca} =0.1,
Loading plate	*MAT_RIGID	ρ= 7850kg/m³, E=200GPa, ν=0.27
Longitudinal rebar, stirrups and screw rod	*MAT_PLASTIC_KINEMATIC	ρ=7850kg/m³, E=210GPa, ν=0.27， f_y=Table 4, E_t=2GPa, F_S=0.45

Note: ρ is mass density; E is Young's modulus; ν is Poisson's ratio; f_y is yield stress; E_t is tangent modulus; F_S is failure strain; f_c is uniaxial compression strength; ERO is eroding strain; $AgS_{\max}$ is maximum aggregate size; E_a, E_b and E_c are Young's modulus in a-direction, b-direction and c-direction, respectively; X_t is longitudinal tensile strength; Y_t is transverse tensile strength ;

Y_c is transverse compressive strength; AOPT is material axes option; v_{ab}, v_{bc} and v_{ca} are Poisson's ratio in *ab*-plane, *bc*-plane and *ca*-plane, respectively.

4.2 Contact

The FE model used the most widely used automatic contact *CONTACT_AUTOMATIC to simulate the relationship between contact pairs. *CONTACT_ERODING_SINGLE_SURFACE was used for interface between drop hammer and loading plate, and that between loading plate and concrete. While *CONTACT_AUTOMATIC_SURFACE_TO_SURFACE is used for interface between support plate and concrete. The friction coefficient FS and FD of the contact surface are set as 0.2, with penalty function coefficients SFS and SFM set as 1.0.

4.3 Modeling of prestress

LS-DYNA provides several methods for introducing prestressing that have been successfully applied to prestressed strands or steel bars, namely the thermal shortening method [22], the direct-tension method [23], and the "Spotweld" method [24]. To perform transient dynamic analysis, the specimens require to be prestressed stably. Based on the installation procedure of anchor, this study proposed two new prestress modeling skills, which are (1) initial stressing of CFRP element and (2) direct tension of screw rod. The initial stressing method for CFRP elements was applied through *INITIAL_STRESS_SHELL_SET, in which CFRP was modeled as a set of shell units. The direction tension of screw rod was applied directly through *INITIAL_STRESS_BEAM and *CONTROL_DYNAMIC_RELAXATION which fully considered the real prestress procedure.

4.4 Framework of multi-impact simulation

There are extensive simulation work for RC structures under single impact [21,25,26], however the simulation of repeated impact has been rarely reported. This study proposed three methods of repeated impact simulation to analyze the residual performance of RC beams after 2nd or 3rd impact. Figure 21 lists the calculation frameworks of each method that could be referred to multiple impacts simulation.

Method I is called Springback Method (Figure 21a). In this method, keyword “SPRINGBACK-LSDYNA” should be used in creating the FE model of the first impact simulation with the “Partset” selected. Then, submit the simulation to obtain the “DYNAIN” file which contains the selected partset’s initial stress, strain and boundary condition information of the first impact. For the second impact simulation, it needs to create a new “K” file and import the above “DYNAIN” file and update a new hammer. Then, submit the model for calculation and output the 2nd impact result, and so on for multiple impacts.

Method II is Multi-hammer Impact Method (Figure 21b). This method allows to create FE model with multiple hammers in LS-DYNA. The hammers were dropped at a specific time with a specified calculated speed according to Energy Conservation Law, requiring keyword "*LOAD_BODY_X/Y/Z" to generate a gravity curve. The dynamic responses calculated by this method can be continuously output.

Method III is Restart Method (Figure 21c). The created FE model should fill in keyword "*DATABASE_BINARY_D3DUMP" save the result after 1st impact. For the second impact, it needs to create a new "K" file and import a new hammer given a new initial velocity. In next step, the model requires to fill in keyword "*STRESS_INITIALIZATION_OPTION" to transmit the initial stress status from " D3DUMP" file to the target model, which is like "prestressed loading". For the part to be initialized, the number of nodes, units, arrangement and topological relationship in the input file should be the same as those in the latest input file. Lastly, submit " D3DUMP" file together with the new "K" file for calculation to obtain the second impact result, and so on. In fact, these three methods could store the initial result data after the 1^{st} impact from different ways, following the 2^{nd} impact, therefore similar results can be obtained using these three methods. Based on the modeling experience, Multi-hammer Impact Method (Method II) has the most fast-track modelling technique and reliable results which is recommended in this study.

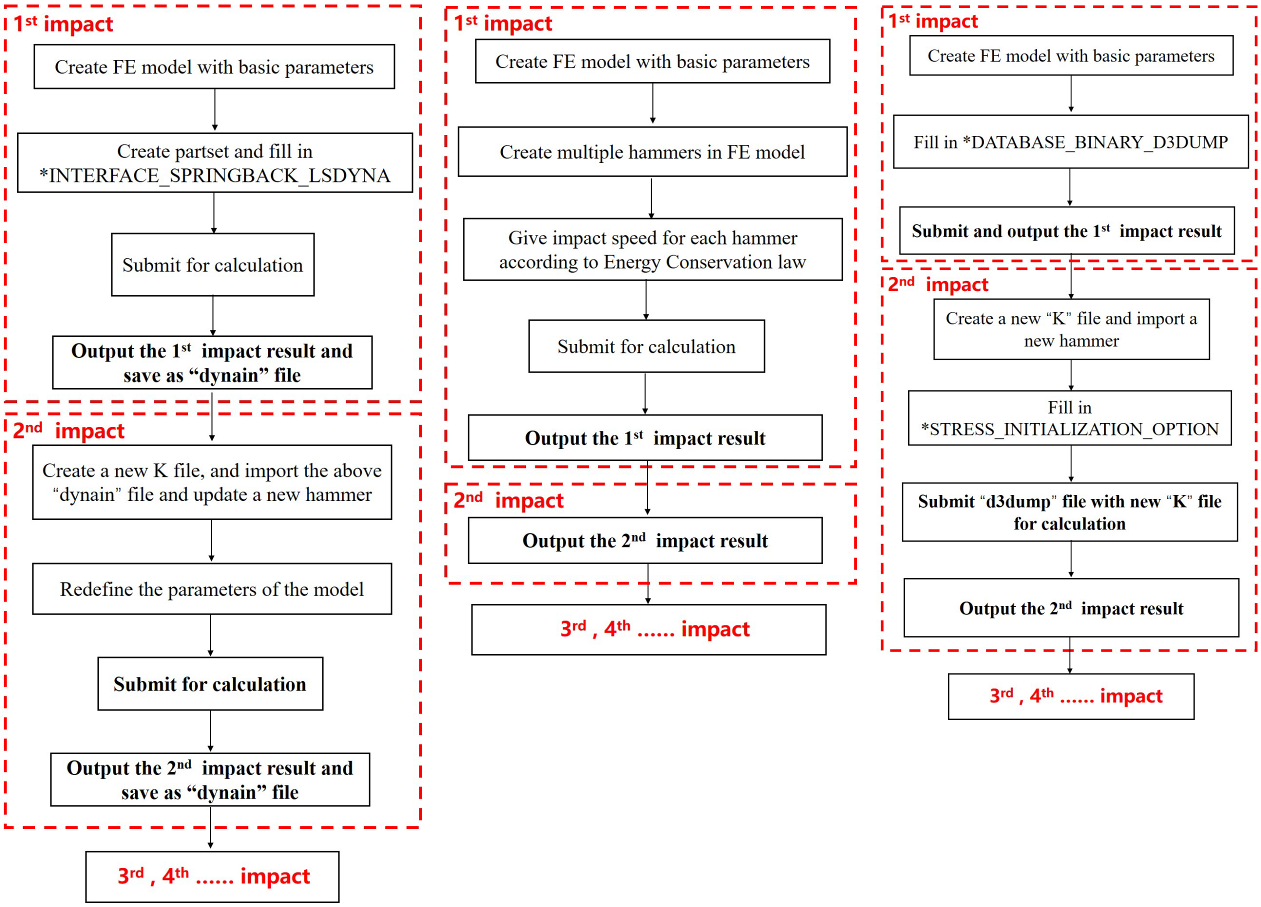

(a) Method I (b) Method II (c) Method III

Figure 21 Methods for multi-impact simulation.

4.5 Comparison between FE and Experiment Results

4.5.1 Crack patterns

Figure 22 shows the typical plastic strain development processes of PRB14-896-2.7 under first and second impact. The different color represents different damage level of concrete or crack pattern. From the strain comparison between the test and simulation of concrete at different times, the FE model can reasonably capture the crack location and damage level of the concrete in the flexural zone.

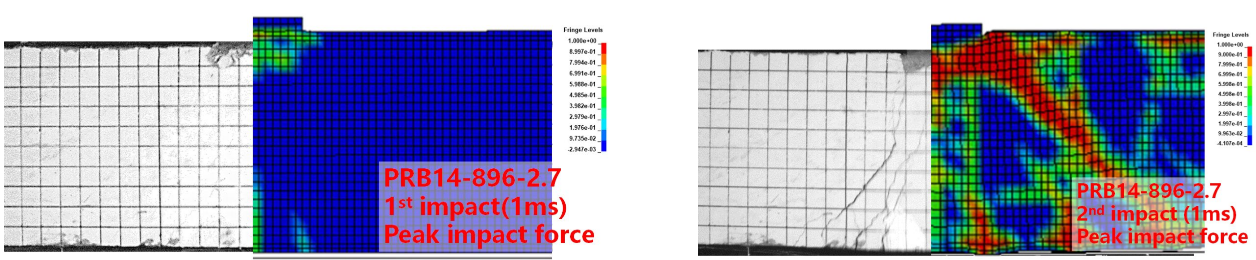

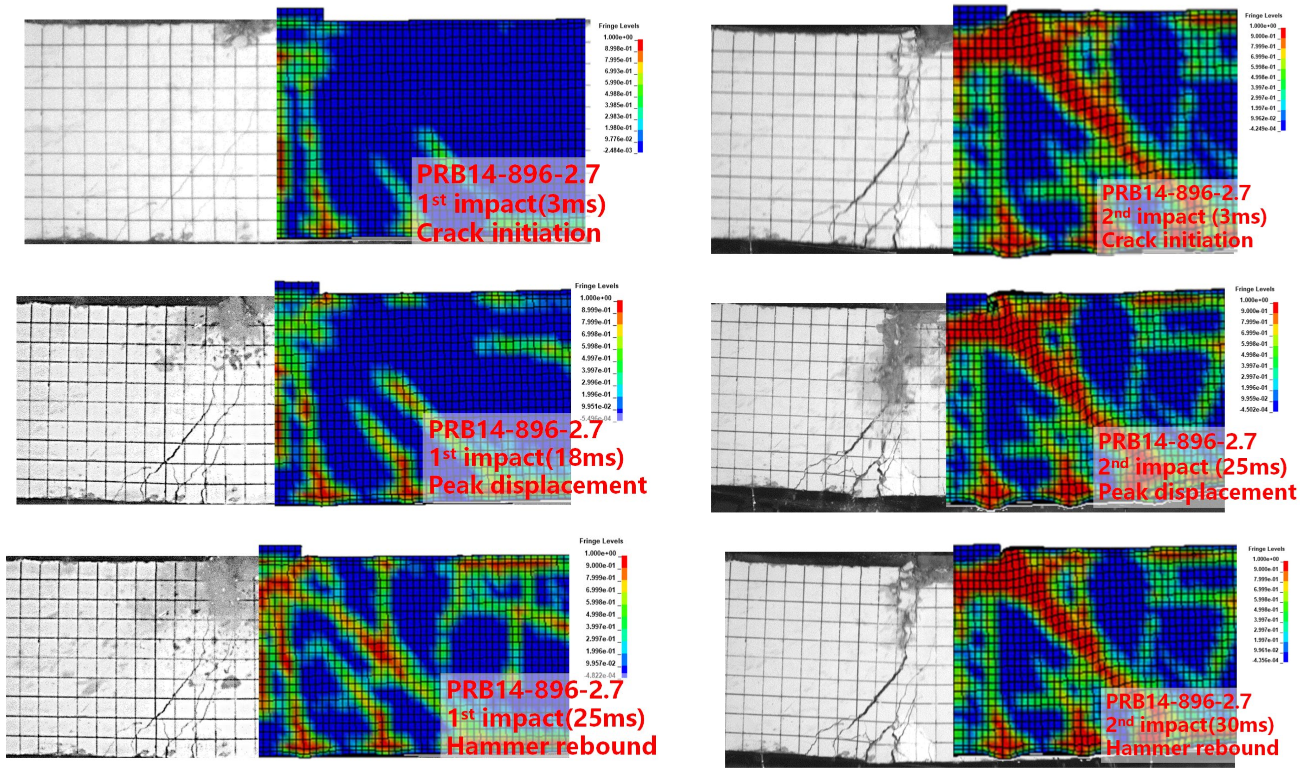

(a) PRB14-896-2.7 subject to 1st impact (b) PRB14-896-2.7 subject to 2nd impact

Figure 22 Crack propagation of RC beams under multi-impacts

4.5.2 Impact force and mid-span displacement histories

Figures 23(a-l) compares the impact force and mid-span displacement history between FE and test results of the specimen under multiple impacts. Generally, the FE model can predict reasonably accurate the impact force and mid-span displacement history of each specimen, which shows that the initial slope, peak point and duration of the curves agree well with the test results. The decline and fluctuation trend of the curves can be well simulated during the impact. However, the amplitude of curve fluctuation and the residual displacement have some deviations. Table 10 lists the peak impact force and mid-span displacement between test and FE results. Under first impact, the average value of PIF_{FE} /PIF ratio and PMD_{FE} /PMD is 7.2% and 15.3% while under second impact, the ratios are 7.8% and 7.1% respectively. It should be noted that the eroding strain of CSCM concrete model in LS-DYNA is set to be 1.6 that is well represented to reproduce reasonably the dynamic responses of RC beams subjected to multi-impact. However, the error between test and simulation may be because the existing concrete constitutive model may not be able to take into account the accumulated damage after repeated impacts. Also, the contact properties and contact algorithm in FE modeling increase the stiffness of contact surface, thus leading to shorten the response time [27]. Generally, the multi-impact modelling methods provided in this study can reasonably capture the dynamic response of specimens, i.e., crack morphology, displacement and impact force history, etc. This will provide an effective reference to similar multi-impacts on other types of structures.

Table 10 Comparison of peak impact force and displacement between test and FE results

Specimen ID	PIF (kN)	PIF$_{_FE}$ (kN)	PIF$_{_FE}$/PIF	PMD (mm)	PMD$_{_FE}$ (mm)	PMD$_{_FE}$/PMD
NB-896-2.7(1st)	1653.5	1764.3	1.07	47.6	37.5	0.79
PRB16-896-2.7(1st)	1610.0	1756.5	1.09	44.6	36.7	0.82
PRB14-896-2.7(1st)	1702.1	1802.5	1.06	42.5	39.5	0.93
Mean.			1.07			0.85
NB-896-2.7(2nd)	1929.8	1673.1	0.87	53.8	60.9	1.12
PRB16-896-2.7(2nd)	1706.3	1771.1	1.04	57.9	61.8	1.06
PRB14-896-2.7(2nd)	1770.3	1883.6	1.06	55.1	57.0	1.03
Mean.			0.99			1.07

NOTE: PIF is Peak Impact Force by test; PIF-FE is Peak Impact Force by FE analysis; PMD is Peak Mid-span Displacement by test; PMD-FE is Mid-span Displacement by FE analysis.

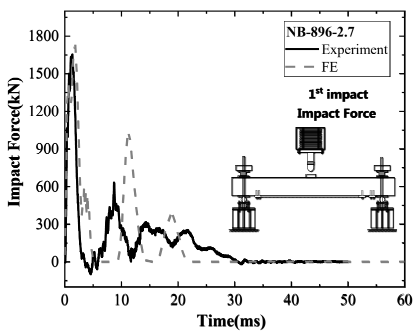

(a)Impact force of NB-896-2.7

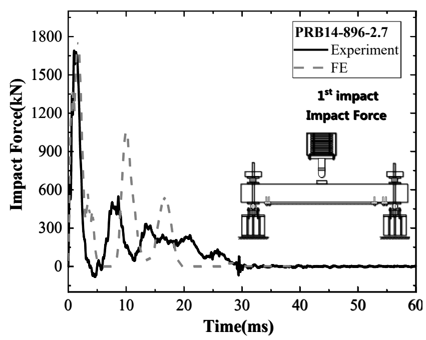

(b)Impact force of PRB14-896-2.7

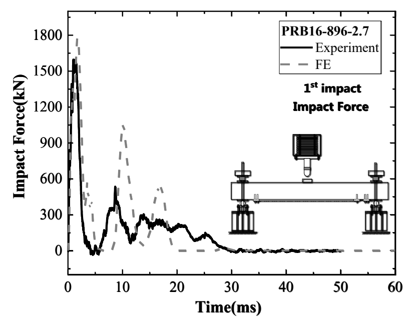

(c)Impact force of PRB16-896-2.7

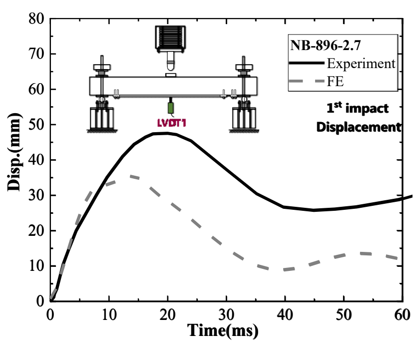

(d)Displacement of NB-896-2.7

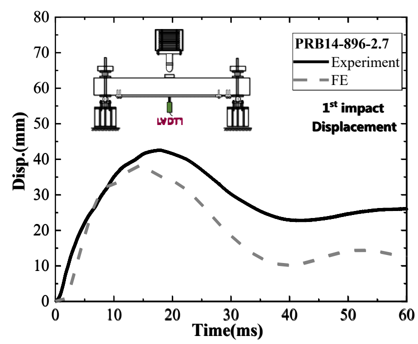

(e)Displacement of PRB14-896-2.7

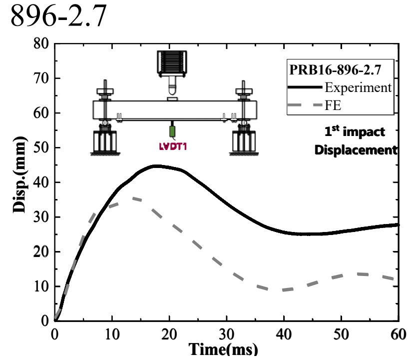

(f)Displacement of PRB16-896-2.7

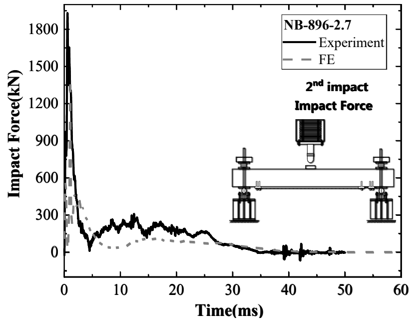

(g)Impact force of NB-896-2.7

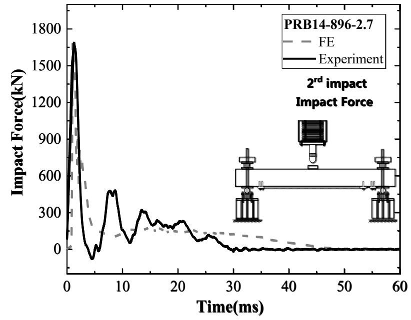

(h)Impact force of PRB14-896-2.7

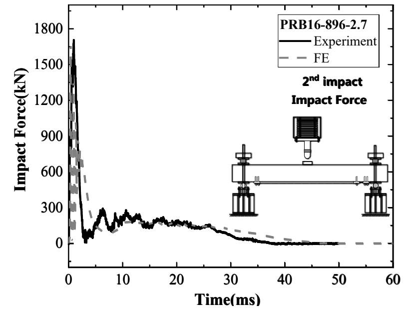

(i)Impact force of PRB16-896-2.7

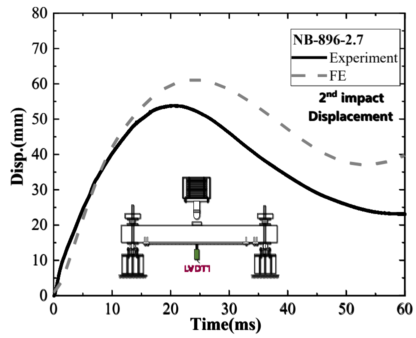

(j)Displacement of NB-896-2.7

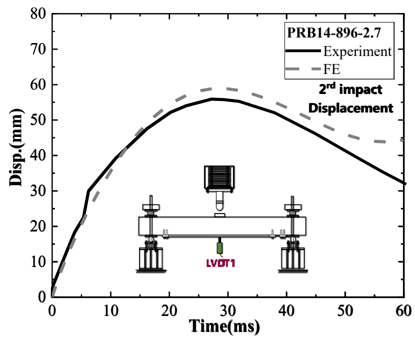

(k)Displacement of PRB14-896-2.7

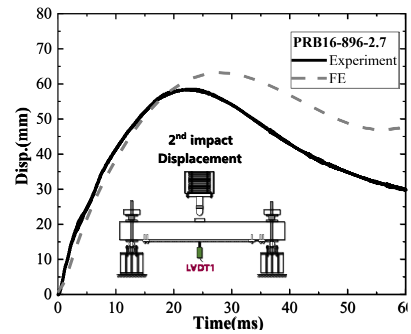

(l)Displacement of PRB16-896-2.7

Figure 23 Comparison of multi-impact responses between test and FE results

5. Conclusions

The present study firstly develops a novel prestressed CFRP strengthened RC beams using H-type end anchor with ductility controllable device to improve the ductility behavior while using CFRP as strengthening material. This study investigates the static and impact performance of prestressed CFRP strengthened RC beams experimentally and numerically. A series of static tests and multi-impact tests have been conducted. Dynamic finite element analysis using LS-DYNA has been performed to validate against the test results. The following conclusions can be drawn from this investigation:

(1) Based on the design of novel H-type anchor, a pre-tension technique has been developed to the strengthening system. It is found that the short-term prestress loss is between 5% - 15%. The higher initial tension prestress, the higher loss of prestress. The bonded prestressed CFRP reinforcement leads to a higher stress loss rate of prestress, thus it is suggested to adopt the self-locking prestressed CFRP reinforcement method without bond.

(2) Four-point bending tests has been conducted on the prestressed CFRP strengthened beams. It is found that unbonded RC beam has 25.9% higher flexural resistance compared to the reference RC beam. The increasing rate of cracking load is higher than the yield and ultimate load. The

ductility coefficient of the unbonded RC beam increases up to 62.6% compared to that of the bonded RC beam.

(3) All the beams fail in typical flexural mode. It is found that the flexural impact failure of NB series beam is more serious than that of PRB series beam. Specifically, the mid-span peak displacement and peak impact load of NB series beam are 10.6% and 2.9% higher than those of PRB series beam, and the number of flexural cracks in mid-span zone appear more pronounced. The strain analysis of the specimens with different screw diameter shows that the composite action of PRB14-896-2.7 exhibits more effective than that of PRB16-896-2.7.

(4) This study proposed two modeling schemes of prestressing CFRP namely initial stress method of shell element and direction tension of screw rod, and summarized a framework of multi-impact simulation including “Spring Back Method”, “Multi-hammer Impact Method” and “Restart Method”. The FE results predicted by these three methods could well simulate the main crack distribution patterns, displacement and impact force history of specimens. Multi-hammer Impact Method provides more fast-track and convenient modelling skills than other methods. The maximum error of peak impact force between FE and test is within 7.8% while the maximum error of peak displacement is within 15.3%, respectively.

(5) There is still some deviation between the FE and test results in terms of the displacement and impact force. This may be because of the existing concrete constitutive model may not be able to consider the accumulative damage of concrete after repeated impacts. Therefore, to improve prediction accuracy, the future study needs to develop a dynamic constitutive model of concrete to consider the cumulative damage effect. This is also required for the complicated impact scenarios.

Acknowledgement

This paper is supported by the project of Key Laboratory of Impact and Safety Engineering (Ningbo University), Ministry of Education. The project number is cj202005. The authors would like to acknowledge the research grant received from the National Natural Science Foundation of China (Grants No. 51978407), Shenzhen Basic Research Project (Grant No. JCYJ20180305124106675), and Guangdong Provincial Key Laboratory of Durability for Marine Civil Engineering (SZU) (Grant No. 2020B1212060074).

References

[1] Li JB, Gong JX, Wang LC. Seismic behavior of corrosion-damaged reinforced concrete columns strengthened using combined carbon fiber-reinforced polymer and steel jacket[J]. Construction and Building Materials, 2009, 23(7):2653-2663.

[2] Lee HS, Tadatsugu Kage, Takafumi Noguchi, Fuminori Tomosawa. An experimental study on the retrofitting effects of reinforced concrete columns damaged by rebar corrosion strengthened with carbon fiber sheets[J]. Cement and Concrete Research, 2003, 33(4):563-570.
[3] Deng Z, Li P. Corrosion Resistance Research of Corrosion-damaged Reinforced Concrete Columns Wrapped With CFRP[J]. Journal of Beijing University of Technology, 2010, 36(1): 18-24. (in chinese)
[4] Tamer El Maaddawy. Behavior of corrosion-damaged RC columns wrapped with FRP under combined flexural and axial loading[J]. Cement and Concrete Composites, 2008, 30(6): 524-534.
[5] Ilg P, Hoehne C, Guenther E. High-performance materials in infrastructure: a review of applied life cycle costing and its drivers–the case of fiber-reinforced composites[J]. Journal of cleaner production, 2016, 112: 926-945.
[6] Burgoyne C, Balafas I. Why is FRP not a financial success[C]//Proc. 8th Intl. Conf. on FRP Reinforcement for Reinforced Concrete Structures, FRPRCS-8, Univ. of Patras, Patras, Greece. 2007.
[7] Naaman A E. FRP reinforcements in structural concrete: assessment, progress and prospects[M]//Fibre-Reinforced Polymer Reinforcement for Concrete Structures: (In 2 Volumes). 2003: 3-24.
[8] Zhou YW, Zheng SB, Huang ZY, Sui LL, Chen Y, Explicit neural network model for predicting FRP-concrete interfacial bond strength based on a large database[J]. Composite Structures, 2020;240, 111998.
[9] Huang ZY, Qian XD, Su ZC, Pham DC, Sridhar N, Adam J.Sobey and AjitShenoi. Experimental Investigation and Damage Simulation of Large-scaled Filament Wound Composite Pipes[J]. Composites Part B. 2020;184,107639.
[10] Zhou YW, Zheng YW, Pan J, Sui LL, Xing F, Sun HF, et al. Experimental investigations on corrosion resistance of innovative steel-FRP composite bars using Xray microcomputed tomography[J]. Compos Part B, 2019;161:272–84.
[11] Huang ZY, Liew JYR. Steel-concrete-steel sandwich composite structures subjected to extreme loads[J]. International Journal of Steel Structures, 2016, 16(4):1009-1028.
[12] Wang B, Zhu HR, Wu XH, Zhang NY, Yan BQ, Numerical investigation on low-velocity impact response of CFRP wraps in presence of concrete substrate[J], Composite Structures. 2020; 231,111541.
[13] Pham TM, Zhang X, Elchalakani M, Karrech A, Hao H, Ryan Aarin. Dynamic response of rubberized concrete columns with and without FRP confinement subjected to lateral impact[J]. Construction and building materials. 2018,186(20):207-218.
[14] Wang R, Han LH, Tao Z. Behavior of FRP–concrete–steel double skin tubular members under lateral impact: Experimental study[J]. Thin-Walled Structures,2015, 95:363-373.
[15] Sina Eskandari, Francisco M. Andrade Pires, Pedro P. Camanho, Hao Cui, Nik Petrinic, Antonio T. Marques. Analyzing the failure and damage of FRP composite laminates under high strain rates considering visco-plasticity[J], Engineering Failure Analysis,101,2019,257-273.
[16] Bhatti A Q, Kishi N, Mikami H, et al. Elasto-plastic impact response analysis of shear-failure-type RC beams with shear rebars[J]. Materials & Design, 2009, 30(3): 502-510.
[17] Liu T, Xiao Y. Impact Behavior of CFRP-Strip–Wrapped RC Beams without Stirrups[J]. Journal of Composites for Construction, 2017, 21(5):04017035.
[18] Al-Zubaidy H, Zhao XL , Al-Mahaidi R. Mechanical characterisation of the dynamic tensile properties of CFRP sheet and adhesive at medium strain rates[J]. Composite Structures, 2013, 96(FEB.):153–164.

[19] Singh N K , Singh K K . Review on impact analysis of FRP composites validated by LS‐DYNA[J]. Polymer Composites, 2015, 36(10):1786-1798.
[20] Chang F K, Chang K Y. A progressive damage model for laminated composites containing stress concentrations[J]. Journal of composite materials, 1987, 21(9): 834-855.
[21] Zhao De-Bo, Yi Wei-Jian, Kunnath Sashi K. Numerical simulation and shear resistance of reinforced concrete beams under impact, Engineering Structures, 2018, 166: 387-401.
[22] Jiang H, Chorzepa M G. An effective numerical simulation methodology to predict the impact response of pre-stressed concrete members[J]. Engineering Failure Analysis, 2015, 55: 63-78.
[23] Chung C H, Lee J, Jung R, et al. Assessment of impact resistance performance of post-tensioned curved wall using numerical impact analysis[J]. Journal of the Computational Structural Engineering Institute of Korea, 2016, 29(2): 161-167.
[24] Thai D K, Kim S E. Numerical simulation of pre-stressed concrete slab subjected to moderate velocity impact loading[J]. Engineering Failure Analysis, 2017, 79: 820-835.
[25] Cotsovos D M , Pavlovic M N . Modelling of RC beams under impact loading[J]. Structures & Buildings, 2012, 165(2):77-94.
[26] Gonzalo S.D. Ulzurrun, Carlos Zanuy.Enhancement of impact performance of reinforced concrete beams without stirrups by adding steel fibers.Construction and Building Materials, 2017, 145: 166-182..
[27] Thong M. Pham, Yifei Hao, Hong Hao, Sensitivity of impact behaviour of RC beams to contact stiffness, International Journal of Impact Engineering, 2018,112,155-164.